

Article

Meson-Exchange Currents in Quasielastic Electron Scattering in a Generalized Superscaling Approach

Paloma Rodriguez Casale^{1,2}, Jose Enrique Amaro^{1,2,*}  and Maria B. Barbaro^{3,4} ¹ Departamento de Física Atómica, Molecular y Nuclear, 18071 Granada, Spain; palomacasale@ugr.es² Instituto Carlos I de Física Teórica y Computacional, Universidad de Granada, 18071 Granada, Spain³ Dipartimento di Fisica, Università di Torino, 10125 Torino, Italy; barbaro@to.infn.it⁴ INFN Sezione di Torino, 10125 Torino, Italy

* Correspondence: amaro@ugr.es

Abstract: We introduce a method for consistently incorporating meson-exchange currents (MEC) within the superscaling analysis with relativistic effective mass, featuring a new scaling variable, ψ^* , and single-nucleon cross-sections derived from the relativistic mean field (RMF) model of nuclear matter. The single-nucleon prefactor is obtained from the $1p1h$ matrix element of the one-body current, combined with the two-body current, averaged over a momentum distribution of Fermi kind. The approach is applied to selected quasielastic cross-sectional data on ^{12}C . The results reveal a departure from scaling behavior, yet, intriguingly, the data collapse into a discernible band that is parametrized using a simple function of ψ^* . This calculation, as developed, is not intended to provide pinpoint precision in extracting nuclear responses. Instead, it offers a global description of the quasielastic data with a considerable level of uncertainty. However, this approach effectively captures the overall trends of the quasielastic data beyond the Fermi gas model with a minimal number of parameters. The model incorporates partially transverse enhancement of the response, as embedded within the relativistic mean field framework. However, it does not account for enhancements attributed to the combined effects of tensor correlations and MEC, given that the initial RMF model lacks these correlations. A potential avenue for improvement involves starting with a correlated Fermi gas model to incorporate additional enhancements into single-nucleon responses. This study serves as a practical demonstration of implementing such corrections.

Keywords: superscaling; quasielastic electron scattering; meson-exchange currents; relativistic mean field



Citation: Casale, P.R.; Amaro, J.E.; Barbaro, M.B. Meson-Exchange Currents in Quasielastic Electron Scattering in a Generalized Superscaling Approach. *Symmetry* **2023**, *15*, 1709. <https://doi.org/10.3390/sym15091709>

Academic Editors: Tomohiro Inagaki and Olga Kodolova

Received: 27 July 2023

Revised: 30 August 2023

Accepted: 4 September 2023

Published: 6 September 2023



Copyright: © 2023 by the authors. Licensee MDPI, Basel, Switzerland. This article is an open access article distributed under the terms and conditions of the Creative Commons Attribution (CC BY) license (<https://creativecommons.org/licenses/by/4.0/>).

1. Introduction

A substantial effort has been devoted to the investigation of the electromagnetic response of nuclei in the quasielastic peak. Following the success of the Fermi gas model in providing a straightforward description of the cross-section, the focus shifted towards the separate response functions bringing to the forefront both experimental challenges in the longitudinal/transverse (L/T) separation and theoretical complexities in their depiction [1,2]. One initial challenge, the quenching of the longitudinal response, has seen theoretical resolution through the inclusion of short-range correlations within the nuclear wave function, along with accounting for final state interactions. This approach also appears to address the associated issue concerning the description of the Coulomb sum rule [3–5].

The situation becomes more intricate when examining the transverse response, as calculations in light nuclei have revealed a positive interference between one-body and two-body currents, resulting in an enhancement of the transverse response compared to what the one-body current alone would predict [6,7]. This enhancement, attributed to meson-exchange currents (MEC), has also been observed in the transverse response of ^{12}C [8] within the Green Function Monte Carlo model [9–11], and it has been parameterized

in a phenomenological fit of the cross-section [12,13]. A calculation by Fabrocini in nuclear matter [14] points towards this enhancement being a result of the simultaneous interaction of tensor nucleon–nucleon correlations with the Δ -isobar exchange current, as independent particle models typically predict negative interference between the one-body current and MEC [15]. For high-momentum transfer ($q > 500$ MeV/c), the situation becomes more complex due to the significant influence of relativistic effects [16,17].

In recent years, there has been a resurgence of interest in electron scattering studies [16,18–21], driven by the potential to calibrate theoretical models using (e, e') data. These calibrated models can then be extended to neutrino interactions by incorporating the contributions of the axial current. The pursuit of neutrino oscillation experiments represents a formidable scientific endeavor, encompassing a synergy of experimental and theoretical efforts [22–27]. Theoretical nuclear physics has taken a central role in analyzing neutrino-induced nuclear reactions within these experiments [28–37]. The objective is to minimize uncertainties stemming from nuclear effects, which constitute a primary source of systematic errors when determining neutrino interactions within detectors. The interplay and relationship between neutrino and electron scattering cross-sections play a pivotal role in this context, serving as a crucial mechanism for controlling and mitigating systematic errors.

At typical energies around 1 GeV in many neutrino experiments, a significant contribution arises from quasielastic nucleon emission, which dominates at transferred energies around $\omega = |Q^2|/2m_N^*$, where ω is the energy transfer, $Q^2 = \omega^2 - q^2 < 0$, and q is the momentum transfer to a nucleon with relativistic effective mass m_N^* [38–42]. It is crucial to take into account that the transferred energies involved in neutrino experiments necessitate a relativistic treatment of the reaction. This requirement introduces significant challenges in constructing appropriate models for these interactions [8,43–46].

In addition, the emission of two particles (2p2h), originating from MEC and short-range correlations, has emerged as a central focus in the study of lepton-nucleus scattering. A significant body of research has been devoted to comprehending the impact of 2p2h processes on the cross-sections of both electron and neutrino interactions [47–57]. The most commonly employed approaches are often based on the Fermi gas and shell models. Refs. [58,59] introduced a generalized formalism rooted in factorization principles and nuclear spectral functions, enabling the treatment of transition matrix elements that incorporate MEC. The framework was further expanded in Ref. [60] to the weak charged and neutral currents. Ab initio methods such as the Green Function Monte Carlo (GFMC) approach, while powerful, encounter a significant challenge in that they are inherently non-relativistic. Extending these methods to cover the entire range of energies and momentum transfers of interest is a non-trivial endeavor [61].

It is often overlooked that MEC also contribute to the emission of a single particle (1p1h), thereby introducing interference effects with the one-body current [16]. Notably, calculations in Fermi gas and shell models have shown a reduction in the quasielastic transverse response compared to the impulse approximation [15,16,62–68]. This reduction is mainly due to the exchange part of the 1p1h matrix element of the Δ current. The negative interference between one-body and two-body currents is a consistent feature in all independent particle models. As mentioned previously, it is only when tensor nucleon–nucleon correlations are incorporated that a positive interference arises [14].

In this work, we present a method for the consistent inclusion of meson-exchange currents (MEC) within the framework of the superscaling analysis with relativistic effective mass (SuSAM*) [69,70]. This scaling approach sets itself apart from the SuSA methodologies [18,36,71–74] offering an alternative means to globally and on average describe (e, e') quasielastic cross-sections.

The scaling models are founded on the premise of approximating nuclear responses as a product of a single-nucleon response, multiplied by a scaling function. The phenomenological scaling function effectively accounts for nuclear structure and reaction effects, with its parameters fitted to experimental data. The motivation behind scaling models arises

from the observation that inclusive data, when divided by an appropriate single-nucleon prefactor, approximately scale when plotted against a suitable scaling variable, ψ , extracted from the relativistic Fermi gas (RFG) model [71]. The SuSA model [34], along with its improved version SuSAv2, and the alternative SuSAM*, has been extensively utilized to analyze inclusive electron and neutrino scattering data [18,36,71–74]. By establishing a phenomenological scaling function extracted from (e, e') data, these models provide a valuable foundation for extrapolating to neutrino cross-sections.

The SuSAM* model used in this work differs from the SuSA framework by incorporating the effective mass dependence from the relativistic mean field (RMF) theory. A notable feature of the RMF model of nuclear matter (such as the Walecka or $\sigma - \omega$ model [39]) is that it reproduces the (e, e') cross-section better than the RFG model when an appropriate value for the effective mass M^* is chosen [38,41,75]. Motivated by this, the SuSAM* model employs the RMF model's scaling variable, ψ^* , and single-nucleon prefactor dependent on the effective mass, with the aim to capture the relativistic dynamics associated with the RMF.

Another distinguishing feature is that, while SuSA assumes distinct longitudinal and transverse scaling functions, in SuSAM*, only a single scaling function is considered. Consequently, all differences between the longitudinal and transverse responses are attributed to the characteristics of the single nucleon. Within SuSAM*, the single nucleon partially accounts for the enhancement of the transverse response through the effective mass [19]. The scaling function is obtained from selected quasielastic cross-section data, after discarding non-scaling data points. The selected quasielastic data are organized into a robust 'thick band', as parameterized in Ref. [19]. The inherent level of uncertainty within this band reflects the extent to which the ψ^* -scaling is violated. This approach yields significant deviations both above and below the average, depending upon the kinematic conditions. Consequently, it should not be regarded as a precise parametrization of the cross-section or a means for pinpoint accuracy in extracting response functions. Rather, its purpose is to offer a global, averaged description of the quasielastic data beyond the FRG. It presents the advantage of simplicity, involving only a limited number of parameters.

Until now, a unified model that incorporates 1p1h MEC in the superscaling approach had not been proposed. This was primarily due to the violation of scaling properties by MEC, even at the Fermi gas level [76]. Additionally, the 1p1h matrix element of MEC is not easily extrapolated to the $|\psi| > 1$ region outside the range where the Fermi gas response is different from zero, as nucleons are constrained by the Fermi momentum. In this work, we address both of these challenges in a unified manner by modifying the SuSAM* model to account for the contribution of MEC within the single-nucleon prefactor. In the new approach, the single-nucleon response is averaged with a smeared momentum distribution around the Fermi surface [77]. As a result, the averaged single-nucleon responses are well-defined for all of the values of ψ^* .

The single-nucleon response now incorporates the contribution of MEC to the effective one-body current operator, enabling a novel scaling analysis of the data. We anticipate that the 1p1h MEC matrix elements, when incorporated within the single-nucleon framework, result in a negative contribution due to our initial assumption of an independent particle model. However, if one were to start from a model that incorporates tensor correlations between nucleons, it could potentially lead to the construction of a single nucleon prefactor featuring the corresponding enhancement of the transverse response. The approach delineated in this paper could be similarly applied in this scenario. The ultimate goal of this approach would be to devise a single-nucleon prefactor that enhances the scaling properties of the quasielastic data.

This article is structured as follows. In Section 2, we introduce the formalism of quasielastic electron scattering within the framework RMF model of nuclear matter, incorporating MEC. In Section 3, we present our unified scaling model that incorporates MEC effects. We describe the modifications made to the conventional scaling approach to account for the contribution of MEC within the single-nucleon prefactor. In Section 4, we

present the results of our calculations and analyses based on the unified scaling model with MEC. Finally, in Section 4, we present the conclusions drawn from our study.

2. Formalism

2.1. Response Functions

We start with the inclusive electron scattering cross-section in plane-wave Born approximation with one-photon exchange. The exchanged photon transfers an energy ω and a momentum \mathbf{q} to the nucleus. The initial electron energy is ϵ_e , the scattering angle is θ , and the final electron energy is $\epsilon'_e = \epsilon_e - \omega$. The double differential cross-section is written in terms of the longitudinal and transverse response functions, $R_L(q, \omega)$ and $R_T(q, \omega)$, respectively, where $q = |\mathbf{q}|$

$$\frac{d\sigma}{d\Omega d\epsilon'} = \sigma_{\text{Mott}}(v_L R_L(q, \omega) + v_T R_T(q, \omega)), \quad (1)$$

where σ_{Mott} is the Mott cross-section and v_L and v_T are the kinematic coefficients defined as

$$v_L = \frac{Q^4}{q^4} \quad (2)$$

$$v_T = \tan \frac{Q^4}{q^4} - \frac{Q^2}{2q^2} \quad (3)$$

with $Q^2 = \omega^2 - q^2 < 0$ the four-momentum transfer. The nuclear response functions are the following combinations of the hadronic tensor

$$R_L = W^{00}, \quad R_T = W^{11} + W^{22}. \quad (4)$$

The inclusive hadronic tensor is constructed from the matrix elements of the electromagnetic current operator $\hat{J}^\mu(\mathbf{q})$ between the initial and final hadronic states:

$$W^{\mu\nu} = \sum_f \overline{\sum_i} \langle f | \hat{J}^\mu(\mathbf{q}) | i \rangle^* \langle f | \hat{J}^\nu(\mathbf{q}) | i \rangle \times \delta(E_f - E_i - \omega), \quad (5)$$

where the sum is performed over the undetected final nuclear states $|f\rangle$ and the average over the initial ground state $|i\rangle$ spin components.

In this work, our approach aims at exploring the scaling symmetry of quasielastic data. This scaling symmetry states that the scaling function, that is, the cross-section divided by an appropriately averaged single-nucleon cross-section and multiplied by a kinematic factor, only depends on a single kinematic variable, ψ , rather than on the three variables (ϵ, q, ω) . The scaling function is approximately the same for all nuclei [70]. The starting point for the scaling analysis is the relativistic Fermi gas (RFG) model, where this symmetry holds exactly. In the case of real nuclei, it is only approximately fulfilled, but it proves to be very useful for analyzing experimental data and performing calculations and predictions.

2.2. 1p1h Hadronic Tensor

In independent particle models, the main contribution to the hadronic tensor in the quasielastic peak comes from the one-particle one-hole (1p1h) final states. As the transferred energy increases, there are contributions from two-particle two-hole (2p2h) emission, the inelastic contribution of pion emission above the pion mass threshold, and the deep inelastic scattering at higher energies. Therefore, the hadronic tensor can be generally decomposed as the sum of the 1p1h contribution and other contributions:

$$W^{\mu\nu} = W_{1p1h}^{\mu\nu} + W_{2p2h}^{\mu\nu} + \dots \quad (6)$$

In this work we focus on the 1p1h response, which in the RFG model, reads

$$W_{1p1h}^{\mu\nu} = \sum_{ph} \langle ph^{-1} | \hat{j}^\mu | F \rangle^* \langle ph^{-1} | \hat{j}^\nu | F \rangle \times \delta(E_p - E_h - \omega) \theta(p - k_F) \theta(k_F - h) \quad (7)$$

where $|p\rangle \equiv |\mathbf{p}s_p t_p\rangle$ and $|h\rangle \equiv |\mathbf{h}s_h t_h\rangle$ are plane-wave states for particles and holes, respectively, and $|F\rangle$ is the RFG ground state with all momenta occupied below the Fermi momentum k_F . The novelty compared to previous works on scaling is that we start from a current operator that is a sum of one-body and two-body operators. This approach allows us to consider the contributions of both the usual electromagnetic current of the nucleon and the meson-exchange currents (MEC) to the 1p1h response:

$$\hat{j}^\mu = \hat{j}_1^\mu + \hat{j}_2^\mu, \quad (8)$$

where \hat{j}_1 represents the one-body (OB) electromagnetic current of the nucleon, while \hat{j}_2 is the two-body MEC. Both currents can generate non-zero matrix elements for 1p1h excitation. MEC are two-body operators and they can induce 1p1h excitation due to the interaction of the hit nucleon with a second nucleon acting as a spectator. The many-body matrix elements of these operators are given by

$$\langle ph^{-1} | \hat{j}_1^\mu | F \rangle = \langle p | \hat{j}_1^\mu | h \rangle \quad (9)$$

for the OB current and

$$\langle ph^{-1} | \hat{j}_2^\mu | F \rangle = \sum_{k < k_F} \left[\langle pk | \hat{j}_2^\mu | hk \rangle - \langle pk | \hat{j}_2^\mu | kh \rangle \right] \quad (10)$$

for the two-body current, where the sum over spectator states (k) is performed over the occupied states in the Fermi gas, considering both the direct and exchange matrix elements. Due to momentum conservation, the matrix element of the OB current between plane waves can be written as

$$\langle p | \hat{j}_1^\mu | h \rangle = \frac{(2\pi)^3}{V} \delta^3(\mathbf{q} + \mathbf{h} - \mathbf{p}) \frac{m_N}{\sqrt{E_p E_h}} j_1^\mu(\mathbf{p}, \mathbf{h}), \quad (11)$$

where V is the volume of the system, m_N is the nucleon mass, $E_p = \sqrt{p^2 + m_N^2}$ and $E_h = \sqrt{h^2 + m_N^2}$ are the on-shell energies of the nucleons involved in the process, and $j_1^\mu(\mathbf{p}, \mathbf{h})$ is the OB current (spin-isospin) matrix

$$j_1^\mu(\mathbf{p}, \mathbf{h}) = \bar{u}(\mathbf{p}) \left(F_1 \gamma^\mu + i \frac{F_2}{2m_N} \sigma^{\mu\nu} Q_\nu \right) u(\mathbf{h}), \quad (12)$$

with F_1 and F_2 being the Dirac and Pauli form factors of the nucleon. In the case of the two-body current, the elementary matrix element can be written in a similar form:

$$\langle p'_1 p'_2 | \hat{j}_2^\mu | p_1 p_2 \rangle = \frac{(2\pi)^3}{V^2} \delta^3(\mathbf{p}_1 + \mathbf{p}_2 + \mathbf{q} - \mathbf{p}'_1 - \mathbf{p}'_2) \times \frac{m_N^2}{\sqrt{E'_1 E'_2 E_1 E_2}} j_2^\mu(\mathbf{p}'_1, \mathbf{p}'_2, \mathbf{p}_1, \mathbf{p}_2). \quad (13)$$

Here $j_2^\mu(\mathbf{p}'_1, \mathbf{p}'_2, \mathbf{p}_1, \mathbf{p}_2)$ is a spin-isospin matrix and it depends on the momenta of the two nucleons in the initial and final state. The two-body current contains the sum of the diagrams shown in Figure 1, including the seagull, pionic, and Δ isobar currents. The

specific form of the two-body current function will be given later when we discuss the MEC model. By inserting (13) into Equation (10) we obtain an expression similar to (11) that resembles the matrix element of an effective one-body (OB) current for the MEC:

$$\langle ph^{-1} | \hat{j}_2^\mu | F \rangle = \frac{(2\pi)^3}{V} \delta^3(\mathbf{q} + \mathbf{h} - \mathbf{p}) \frac{m_N}{\sqrt{E_p E_h}} j_2^\mu(\mathbf{p}, \mathbf{h}). \quad (14)$$

Here the effective OB current generated by the MEC involves a sum over the spectator nucleons and is defined by

$$j_2^\mu(\mathbf{p}, \mathbf{h}) \equiv \sum_{k < k_F} \frac{m_N}{V E_k} \left[j_2^\mu(\mathbf{p}, \mathbf{k}, \mathbf{h}, \mathbf{k}) - j_2^\mu(\mathbf{p}, \mathbf{k}, \mathbf{k}, \mathbf{h}) \right]. \quad (15)$$

Note that in the thermodynamic limit $V \rightarrow \infty$, the above sum will be transformed into an integral over the momenta occupied in the Fermi gas:

$$\frac{1}{V} \sum_{k < k_F} \rightarrow \sum_{s_k t_k} \int \frac{d^3 k}{(2\pi)^3} \theta(k_F - k). \quad (16)$$

Finally, we can write the transition matrix element of the total current between the ground state and the 1p1h state as

$$\langle ph^{-1} | \hat{j}^\mu | F \rangle = \frac{(2\pi)^3}{V} \delta^3(\mathbf{q} + \mathbf{h} - \mathbf{p}) \frac{m_N}{\sqrt{E_p E_h}} j^\mu(\mathbf{p}, \mathbf{h}), \quad (17)$$

where the effective total current for the 1p1h excitation includes contributions from both the one-body current and MEC:

$$j^\mu(\mathbf{p}, \mathbf{h}) = j_1^\mu(\mathbf{p}, \mathbf{h}) + j_2^\mu(\mathbf{p}, \mathbf{h}). \quad (18)$$

By inserting (17) into Equation (7) and taking the thermodynamic limit, we obtain the following expression for the hadronic tensor:

$$W^{\mu\nu} = \frac{V}{(2\pi)^3} \int d^3 h \delta(E_p - E_h - \omega) \frac{m_N^2}{E_p E_h} 2w^{\mu\nu}(\mathbf{p}, \mathbf{h}) \times \theta(p - k_F) \theta(k_F - h), \quad (19)$$

where $\mathbf{p} = \mathbf{h} + \mathbf{q}$ by momentum conservation after integration over \mathbf{p} . The function $w^{\mu\nu}$ is the effective single-nucleon hadronic tensor in the transition

$$w^{\mu\nu}(\mathbf{p}, \mathbf{h}) = \frac{1}{2} \sum_{s_p s_h} j^\mu(\mathbf{p}, \mathbf{h})^* j^\nu(\mathbf{p}, \mathbf{h}). \quad (20)$$

In this equation, we did not include the sum over isospin $t_p = t_h$. Therefore, $w^{\mu\nu}$ refers to the tensor of either proton or neutron emission, and the total tensor would be the sum of the two contributions. Note that the effective single-nucleon tensor $w^{\mu\nu}$ includes the contribution of MEC, thus encompassing an interference between the one-body and two-

body currents. Indeed, the relevant diagonal components of the effective single-nucleon hadronic tensor for the longitudinal and transverse responses (4) can be expanded as

$$\begin{aligned} w^{\mu\mu}(\mathbf{p}, \mathbf{h}) &= \frac{1}{2} \sum_{s_p s_h} |j_1^\mu + j_2^\mu|^2 \\ &= \frac{1}{2} \sum |j_1^\mu|^2 + \text{Re} \sum (j_1^\mu)^* j_2^\mu + \frac{1}{2} \sum |j_2^\mu|^2 \\ &\equiv w_1^{\mu\mu} + w_{12}^{\mu\mu} + w_2^{\mu\mu} \end{aligned} \quad (21)$$

where $w_1^{\mu\mu}$ is the tensor corresponding to the one-body current, $w_{12}^{\mu\mu}$ represents the interference between the one-body and two-body currents, and $w_2^{\mu\mu}$ corresponds to the contribution of the two-body current alone. The one-body part is the leading contribution in the quasielastic peak, while the dominant contribution of the MEC corresponds to the interference with the one-body current [15,62], with the pure contribution of the two-body current being generally smaller.

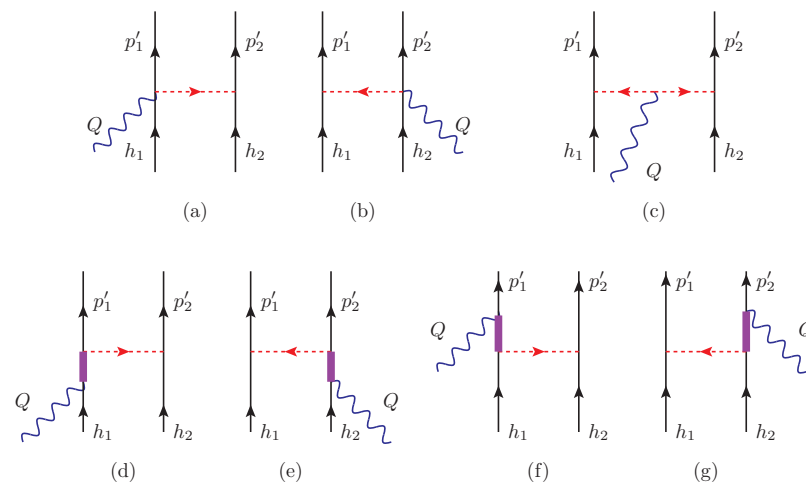


Figure 1. Feynman diagrams for the 2p2h MEC model used in this work. The total MEC are the sum of seagull (diagrams **a,b**), pion in flight (diagram **c**) and Δ current (diagrams **d–g**).

2.3. Responses in the Relativistic Mean Field Approach

Going beyond the relativistic Fermi gas (RFG) model, the relativistic mean field (RMF) approach for nuclear matter allows for the inclusion of dynamic relativistic effects. The simplest approximation in this framework is to introduce constant mean scalar and vector potentials with which the nucleons interact [38,39,41,42]. The scalar potential is attractive, while the vector potential is repulsive. The single-particle wave functions still exhibit plane-wave behavior with momentum p in nuclear matter, but with an on-shell energy given by

$$E = \sqrt{m_N^{*2} + p^2}, \quad (22)$$

where m_N^* is the relativistic effective mass of the nucleon, defined as

$$m_N^* = m_N - g_s \phi_0 = M^* m_N. \quad (23)$$

Here ϕ_0 is the scalar potential energy of the RMF and g_s the corresponding coupling constant [39], and $M^* = 0.8$ for ^{12}C , the nucleus considered in this work [56]. To account for the interaction with the vector potential, a positive energy term needs to be added to the on-shell energy. Therefore, the total energy of the nucleon can be expressed as:

$$E_{RMF} = E + E_v. \quad (24)$$

In this work, we use the value $E_v = 141$ MeV, obtained in Ref. [56] for ^{12}C . Note that in observables that only depend on the energy differences between initial and final particles, the vector energy is canceled out, and only the on-shell energy appears. This cancellation happens, as we will see, in the response associated to the one-body current. However, in the case of the two-body current, the vector energy needs to be taken into account in the Δ current, as we will see in the next section.

In the present RMF approach of nuclear matter, the evaluation of the hadronic tensor is conducted similarly to the RFG, with the difference being that the spinors $u(p)$ now correspond to the solutions of the Dirac equation with the relativistic effective mass m_N^* . From Equation (19), the 1p1h nuclear response functions are then given by

$$R_K(q, \omega) = \frac{V}{(2\pi)^3} \int d^3h \frac{(m_N^*)^2}{E_p E_h} 2w_K(\mathbf{p}, \mathbf{h}) \times \theta(p - k_F) \theta(k_F - h) \delta(E_p - E_h - \omega), \quad (25)$$

where E_p, E_h are the on-shell energies with effective mass m_N^* , and w_K are the single-nucleon responses for the 1p1h excitation

$$w_L = w^{00}, \quad w_T = w^{11} + w^{22}. \quad (26)$$

The effective single-nucleon tensor $w^{\mu\nu}$ is constructed as in Equation (20), but the current is obtained from matrix elements using spinors with the relativistic effective mass m_N^* instead of the normal nucleon mass. This prescription is also followed when evaluating the 1p1h matrix elements of the MEC (as discussed in the next section).

To compute the integral (25), we change to the variables (E_h, E_p, ϕ) , using $h^2 dh d\cos\theta = (E_h E_p / q) dE_h dE_p$. Then the integral over E_p can be performed using the Dirac delta. This fixes the angle θ_h between \mathbf{q} and \mathbf{h}

$$\cos\theta_h = \frac{2E_h\omega + Q^2}{2hq}. \quad (27)$$

The integration over the angle ϕ gives 2π by symmetry of the responses when \mathbf{q} is on the z-axis [35]. The result is an integral over the initial nucleon energy

$$R_K(q, \omega) = \frac{V}{(2\pi)^3} \frac{2\pi m_N^{*3}}{q} \int_{\epsilon_0}^{\infty} d\epsilon n(\epsilon) 2w_K(\epsilon, q, \omega), \quad (28)$$

where we define the adimensional energies $\epsilon = E_h/m_N^*$ and $\epsilon_F = E_F/m_N^*$. Moreover, we introduce the energy distribution of the Fermi gas $n(\epsilon) = \theta(\epsilon_F - \epsilon)$. The lower limit of the integral (28), ϵ_0 , represents the minimum energy that an on-shell nucleon can have when it absorbs energy ω and momentum q [35]

$$\epsilon_0 = \text{Max} \left\{ \kappa \sqrt{1 + \frac{1}{\tau}} - \lambda, \epsilon_F - 2\lambda \right\}, \quad (29)$$

where we define the dimensionless variables

$$\lambda = \frac{\omega}{2m_N^*}, \quad \kappa = \frac{q}{2m_N^*}, \quad \tau = \kappa^2 - \lambda^2. \quad (30)$$

From Equation (28), the nucleons that contribute to the response function $R_K(q, \omega)$ are those with energy ranging from ϵ_0 to ϵ_F . For fixed values of ϕ, q, ω , the integral over energy ϵ in Equation (28) corresponds to integrating the single-nucleon response over a path in the momentum space of the hole \mathbf{h} , weighted with the momentum distribution. The angle between \mathbf{h} and \mathbf{q} for each energy is given by Equation (27). The minimum momentum h_0 corresponds to the minimum energy ϵ_0 . Indeed, for a specific value of ω , the lower limit of

the integral becomes $h = 0$ or $\epsilon_0 = 1$, which corresponds to the center of the quasielastic peak. Using Equation (29), it is straightforward to verify that this point corresponds to $\lambda = \tau$ in the regime without Pauli blocking.

2.4. Scaling

Scaling is based on the approximated factorization of an averaged single-nucleon response from the nuclear cross-section. This factorization is exact in the RMF model with the OB current. In previous works, analytical expressions were obtained from the RFG and RMF models by explicit integration of the one-body responses, Equation (28). However in this case, it is not possible to perform the integration (28) analytically because now w_K also includes the matrix elements of the two-body operator. Nevertheless, we can still define averaged single-nucleon responses as

$$\bar{w}_K(q, \omega) = \frac{\int_{\epsilon_0}^{\infty} d\epsilon n(\epsilon) w_K(\epsilon, q, \omega)}{\int_{\epsilon_0}^{\infty} d\epsilon n(\epsilon)} \tag{31}$$

and we can rewrite Equation (28) in the form

$$R_K(q, \omega) = \frac{V}{(2\pi)^3} \frac{2\pi m_N^{*3}}{q} 2\bar{w}_K(q, \omega) \int_{\epsilon_0}^{\infty} d\epsilon n(\epsilon). \tag{32}$$

The averaged single-nucleon responses, $\bar{w}_K(q, \omega)$, include the combined effect of both the OB current and the MEC in all the 1p1h excitations compatible with given values of (q, ω) . Equation (32) shows that in the RMF model (or the RFG model for effective mass $M^* = 1$), the nuclear responses factorize as the product of the averaged single-nucleon response (including MEC) and the scaling function. In fact, a superscaling function can be defined as

$$f^*(\psi^*) = \frac{3}{4} \frac{1}{\epsilon_F - 1} \int_{\epsilon_0}^{\infty} n(\epsilon) d\epsilon, \tag{33}$$

where $\epsilon_F - 1$ is the kinetic Fermi energy in units of m_N^* and the ψ^* -scaling variable is related to the minimum nucleon energy, ϵ_0 , as

$$\psi^* = \sqrt{\frac{\epsilon_0 - 1}{\epsilon_F - 1}} \text{sgn}(\lambda - \tau). \tag{34}$$

The scaling variable, ψ^* , is negative (positive) for $\lambda < \tau$ ($\lambda > \tau$). In the RMF, the scaling function is easily evaluated from Equation (33), giving

$$f^*(\psi^*) = \frac{3}{4} (1 - \psi^{*2}) \theta(1 - \psi^{*2}). \tag{35}$$

Note that the scaling function of nuclear matter is zero for $\epsilon_0 > \epsilon_F$, and this is equivalent to $|\psi^*| > 1$. This is a consequence of the maximum momentum k_F for the nucleons in nuclear matter, which implies that $\epsilon_0 < \epsilon_F$.

Using $V/(2\pi)^3 = N/(\frac{8}{3}\pi k_F^3)$ for nuclear matter, we can write the response functions (32) as

$$R_K(q, \omega) = \frac{\epsilon_F - 1}{m_N^* \eta_F^3} (Z \bar{w}_K^p(q, \omega) + N \bar{w}_K^n(q, \omega)) f^*(\psi^*), \tag{36}$$

where we add the contribution of Z protons and N neutrons to the response functions, and $\eta_F = k_F/m_N^*$.

2.5. SuSAM*

The expression given by Equation (36) for the response function is formally the same as the response in the RMF, the only difference being that the averaged single-nucleon response now includes the contribution of MEC to the 1p1h excitation. This equation, valid

for the RMF, serves as the starting point for performing the superscaling analysis with relativistic effective mass (SuSAM*) using electron scattering data, extending the formula to the region $\epsilon_0 > \epsilon_F$ or $|\psi^*| > 1$. We follow the procedure suggested by Casale et al. [77].

In the Fermi gas, it is not possible to extend the averaging formula for $\epsilon_0 > \epsilon_F$ because the momentum distribution is zero and the denominator in (31) vanishes. Therefore, we slightly modify the Fermi gas distribution by allowing a smeared Fermi surface, so that the distribution is not exactly zero above k_F , allowing for the averaging procedure. By substituting the Fermi distribution with a distribution that is not significantly different from the original one for $h < k_F$, the average of the single-nucleon response will not change significantly in the Fermi gas region $|\psi^*| < 1$.

By this method, the extension of the single-nucleon average is carried out smoothly and continuously to the region $|\psi^*| > 1$, with the added meaning that, in this way, we take into account, at least partially, the high-momentum distribution. This is because it is primarily the nucleons with momenta greater than k_F that contribute to this region. A possible distribution that can be used to extend the averaging procedure is the Fermi distribution:

$$n(h) = \frac{a}{1 + e^{(h-k_F)/b}}. \quad (37)$$

Using this distribution, the integrals in the numerator and denominator of Equation (31) extend to infinity and are well-defined for $\epsilon_0 > \epsilon_F$ or $|\psi^*| > 1$. An appropriate value for the smearing parameter is $b = 50$ MeV/c, used in Ref. [77], where the averaged single-nucleon responses were evaluated for the one-body current, and it was found to yield practically the same results as the analytically calculated responses in the strict Fermi gas region. The averaged responses were also found to be very similar to the traditionally extrapolated responses outside this region. This proposed method provides a simple approach that allows for the definition of generalized scaling, including the MEC, consistently, and also takes into account that the nucleons are not limited by a maximum Fermi momentum.

Several approaches exist to obtain a phenomenological scaling function. Different methods are based on different assumptions for the scaling function or the single-nucleon response, but all are ultimately adjusted to experimental data. The original SuSA model, based on the RFG, was fitted to the scaling data of the longitudinal response, to obtain a longitudinal scaling function, f_L , while in the extended SuSA-v2 approach, the RMF model for finite nuclei was used to obtain a transverse scaling function, f_T . The SuSAM* model, based on the nuclear matter RMF with effective mass, directly fitted the quasielastic data of the cross-section after discarding the non-scaling data points, to obtain a single phenomenological scaling function valid for both the L and T channels [19]. In the RMF framework, there is an inherent enhancement of the transverse response due to the amplification of the lower component of the spinors by the introduction of the effective mass in the single-nucleon responses. This enhancement was previously demonstrated in Ref. [19]. In the SuSAv2 model, it was accounted for by modifying the transverse scaling function using the RMF theoretical scaling function, as discussed in [18]. In our case, this enhancement is integrated into the single-nucleon transverse response through the effective mass.

In the generalized SuSAM* model proposed here, we follow the same procedure as described in References [42,43]. First, we subtract the calculated inclusive cross-section for two-particle emission in the RMF with a relativistic MEC model from the (e,e') data. This subtraction aims to partially remove the contribution of 2p2h processes present in the data, in order to isolate the purely quasielastic data as much as possible. Next, we scale each residual data point by dividing it by the contribution of the single nucleon to the cross-section, as given by Equation (36),

$$f_{exp}^* = \frac{\left(\frac{d\sigma}{d\Omega d\omega}\right)_{exp} - \left(\frac{d\sigma}{d\Omega d\omega}\right)_{2p2h}}{\sigma_M(v_L r_L + v_T r_T)}, \quad (38)$$

where the single-nucleon cross-section includes the averaged single-nucleon responses including MEC

$$r_K = \frac{\epsilon_F - 1}{m_N^* \eta_F^3 \kappa} (Z \bar{w}_K^p(q, \omega) + N \bar{w}_K^n(q, \omega)). \quad (39)$$

Note that f_{exp} is not solely an experimental quantity, as it inherently depends on the model used to calculate the contribution of the MEC 2p2h processes.

In the results section, we proceed with the scaling analysis for the obtained f_{exp}^* data, using a plot as a function of ψ^* , calculated using Equation (34). This analysis includes a selection process to identify the data points that are most likely to be quasielastic (which exhibit approximate scaling behavior) and discarding the remaining data points (mainly non-scaling inelastic processes). The selection process is based on the assumption that the true quasielastic points approximately scale and tend to collapse into a narrow band. The selection algorithm is described in the Results section when discussing the scaling analysis. Finally, we fit a phenomenological scaling function to the surviving data points, aiming to describe the global scaling behavior of the quasielastic region.

2.6. Meson-Exchange Currents

In this work, we use the relativistic meson-exchange currents (MEC) model described in Ref. [55]. The Feynman diagrams shown in Figure 1 illustrate the different components of the MEC model. Diagrams (a) and (b) correspond to the seagull current, diagram (c) represents the pion-in-flight current, and diagrams (d,e) and (f,g) depict the forward- and backward- $\Delta(1232)$ currents, respectively. The specific treatment of the Δ current is model-dependent, and various versions exist with possible corrections to the off-shell relativistic interaction of the Δ . Other widely used models for MEC include those described in Refs. [54,62,78].

While these different models may exhibit slight variations and corrections to the Δ off-shell interaction, they generally yield similar results for the dominant transverse response at the quasielastic peak. In particular, in the Results section, we compare our findings with the model presented in Refs. [62,78], which we previously employed to assess the impact of MEC on the 1p1h response.

In our model, the MEC functions defined in Equation (13) correspond to the sum of the diagrams of Figure 1

$$j_2^\mu(\mathbf{p}'_1, \mathbf{p}'_2, \mathbf{p}_1, \mathbf{p}_2) = j_{sea}^\mu + j_\pi^\mu + j_\Delta^\mu, \quad (40)$$

where the Δ current is the sum of the forward and backward terms

$$j_\Delta^\mu = j_{\Delta F}^\mu + j_{\Delta B}^\mu. \quad (41)$$

These functions are defined by

$$j_{sea}^\mu = [I_z]_{t'_1 t'_2, t_1 t_2} \frac{f^2}{m_\pi^2} V_{\pi NN}^{s'_1 s_1}(p'_1, p_1) F_{\pi NN}(k_1^2) \bar{u}_{s'_2}(p'_2) F_1^V \gamma^5 \gamma^\mu u_{s_2}(p_2) + (1 \leftrightarrow 2) \quad (42)$$

$$j_\pi^\mu = [I_z]_{t'_1 t'_2, t_1 t_2} \frac{f^2}{m_\pi^2} F_1^V V_{\pi NN}^{s'_1 s_1}(p'_1, p_1) V_{\pi NN}^{s'_2 s_2}(p'_2, p_2) (k_1^\mu - k_2^\mu) \quad (43)$$

$$j_{\Delta F}^\mu = [U_z^F]_{t'_1 t'_2, t_1 t_2} \frac{f f^*}{m_\pi^2} V_{\pi NN}^{s'_2 s_2}(p'_2, p_2) F_{\pi N \Delta}(k_2^2) \bar{u}_{s'_1}(p'_1) k_2^\alpha G_{\alpha\beta}(p_1 + Q) \Gamma^{\beta\mu}(Q) u_{s_1}(p_1) + (1 \leftrightarrow 2) \quad (44)$$

$$j_{\Delta B}^\mu = [U_z^B]_{t'_1 t'_2, t_1 t_2} \frac{f^2 f^*}{m_\pi^2} V_{\pi NN}^{s'_2 s_2}(p'_2, p_2) F_{\pi N \Delta}(k_2^2) \bar{u}_{s'_1}(p'_1) k_2^\beta \hat{\Gamma}^{\mu\alpha}(Q) G_{\alpha\beta}(p'_1 - Q) u_{s_1}(p_1) + (1 \leftrightarrow 2) \quad (45)$$

We evaluate these matrix elements in the framework of the RMF model, where the spinors $u(p)$ are the solutions of the Dirac equation with relativistic effective mass m_N^* . The four-vectors $k_i^\mu = p_i'^\mu - p_i^\mu$ with $i = 1, 2$ are the momenta transferred to the nucleons 1, 2.

We define the following function that includes the πNN vertex, a form factor, and the pion propagator

$$V_{\pi NN}^{s'_1 s_1}(p'_1, p_1) = F_{\pi NN}(k_1^2) \frac{\bar{u}(p'_1) \gamma^5 k_1 u(p_1)}{k_1^2 - m_\pi^2}. \quad (46)$$

We apply strong form factors at the pion absorption/emission vertices given by [47,79]

$$F_{\pi NN}(k) = F_{\pi N\Delta}(k) = \frac{\Lambda^2 - m_\pi^2}{\Lambda^2 - k^2}. \quad (47)$$

The charge structure of the MEC involves the isospin matrix element of the operators

$$I_z = i[\tau(1) \times \tau(2)]_z, \quad (48)$$

$$U_z^F = \sqrt{\frac{3}{2}} \sum_{i=1}^3 (T_i T_z^\dagger) \otimes \tau_i, \quad (49)$$

$$U_z^B = \sqrt{\frac{3}{2}} \sum_i^3 (T_z T_i^\dagger) \otimes \tau_i, \quad (50)$$

where we denote by T_i^\dagger the Cartesian coordinates of the $\frac{1}{2} \rightarrow \frac{3}{2}$ transition isospin operator.

For the transition from a nucleon to a Δ resonance, the isospin transition operator can be represented using the Clebsch–Gordan coefficients, which describe the coupling of isospin 1/2 with isospin 1 to give isospin 3/2 [80]

$$\langle \frac{3}{2} t_\Delta | T_\mu^\dagger | \frac{1}{2} t \rangle = \langle \frac{1}{2} t_1 \mu | \frac{3}{2} t_\Delta \rangle \quad (51)$$

with T_μ^\dagger being the spherical components of the vector \vec{T}^\dagger . With the aid of the expression $T_i T_j^\dagger = (2/3)\delta_{ij} - \frac{i}{3}\tau_i \tau_j$ and making the summation, we can rewrite the isospin operators in the forward and backward Δ current as

$$U_z^F = \sqrt{\frac{3}{2}} \left(\frac{2}{3} \tau_z^{(2)} - \frac{i}{3} [\tau^{(1)} \times \tau^{(2)}]_z \right) \quad (52)$$

$$U_z^B = \sqrt{\frac{3}{2}} \left(\frac{2}{3} \tau_z^{(2)} + \frac{i}{3} [\tau^{(1)} \times \tau^{(2)}]_z \right). \quad (53)$$

The $\gamma N \rightarrow \Delta$ transition vertex in the forward Δ current is defined as [81,82]

$$\Gamma^{\beta\mu}(Q) = \frac{C_3^V}{m_N} (g^{\beta\mu} \not{Q} - Q^\beta \gamma^\mu) \gamma_5 \quad (54)$$

while for the backward Δ current

$$\hat{\Gamma}^{\mu\alpha}(Q) = \gamma^0 [\Gamma^{\alpha\mu}(-Q)]^\dagger \gamma^0. \quad (55)$$

In this vertex, we neglect the contributions of order $O(1/m_N^2)$. Note that the $\Gamma^{\beta\mu}$ operator is a spin matrix and depends on the vector form factor C_3^V . In this paper, we use the vector form factor in Δ current from Refs. [52,82]:

$$C_3^V(Q^2) = \frac{2.13}{(1 - \frac{Q^2}{M_\Delta^2})^2} \frac{1}{1 - \frac{Q^2}{4M_\Delta^2}}. \quad (56)$$

Various alternative approximations to the propagator have been proposed [83]. However, in the case of the quasielastic peak, the typical kinematics are of the order of 1 GeV, and these issues are not expected to be relevant. They are overshadowed by other more sig-

nificant nuclear effects that dominate in this energy regime. Here we use the Δ propagator commonly used for the spin-3/2 field

$$G_{\alpha\beta}(P) = \frac{\mathcal{P}_{\alpha\beta}(P)}{P^2 - M_\Delta^2 + iM_\Delta\Gamma(P^2) + \frac{\Gamma(P^2)^2}{4}} \quad (57)$$

where M_Δ and Γ are the Δ mass and width, respectively. The projector $\mathcal{P}_{\alpha\beta}(P)$ over spin-3/2 on-shell particles is given by

$$\begin{aligned} \mathcal{P}_{\alpha\beta}(P) &= -(\not{P} + M_\Delta) \\ &\times \left[g_{\alpha\beta} - \frac{\gamma_\alpha\gamma_\beta}{3} - \frac{2P_\alpha P_\beta}{3M_\Delta^2} + \frac{P_\alpha\gamma_\beta - P_\beta\gamma_\alpha}{3M_\Delta} \right]. \end{aligned} \quad (58)$$

Finally, the Δ width $\Gamma(P^2)$ is given by

$$\Gamma(P^2) = \Gamma_0 \frac{m_\Delta}{\sqrt{P^2}} \left(\frac{p_\pi}{p_\pi^{res}} \right)^3. \quad (59)$$

In the above equation, p_π is the momentum of the final pion resulting from the Δ decay, p_π^{res} is its value at resonance ($P^2 = m_\Delta^2$), and $\Gamma_0 = 120$ MeV is the width at rest. The width (59) corresponds to the Δ in a vacuum, and it is expected to be slightly different in the medium depending on the kinematics. One could investigate the dependence of the results on the choice of the width. However, in this work, we do not delve into this issue because, as we will see, the effect of the MEC on the 1p1h response is generally small, and corrections due to fine-tuning of the model are unlikely to substantially alter the results.

In the relativistic mean field description used in this work, we consider that the Δ also interacts with the scalar and vector fields, acquiring an effective mass and vector energy. To treat this case, we make the following substitutions in the Δ propagator for the Δ mass and momentum [41,84]:

$$M_\Delta \rightarrow M_\Delta^*, \quad P^{*\mu} = P^\mu - \delta_{\mu 0} E_v^\Delta. \quad (60)$$

We use the value $M_\Delta^* = 1042$ MeV, taken from [57], and the universal vector coupling $E_v^\Delta = E_v$.

With the MEC current defined in Equations (24)–(27), the effective one-body current $j_2(\mathbf{p}, \mathbf{h})$ is generated by summing over the spin, isospin, and momentum of the spectator nucleon, as in Equation (15). First, it can be observed that due to the sum over isospin t_k , the direct term is zero (see Ref. [62] for details). Therefore, the many-body diagrams that contribute to the 1p1h MEC are those shown in Figure 2. Furthermore, it can be verified that diagrams f and g in Figure 2 are also zero. Therefore, only diagrams a, b, c, d, and e in Figure 2 survive and contribute to the 1p1h MEC matrix elements.

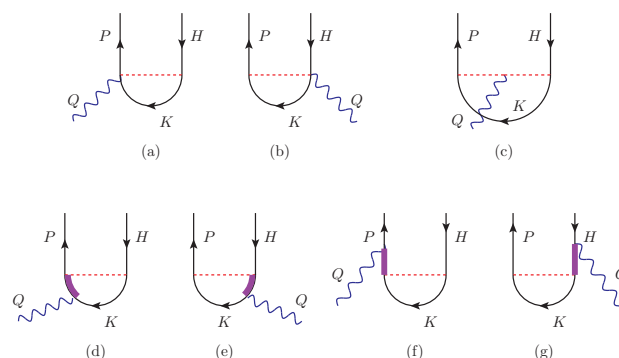


Figure 2. Diagrams for the 1p1h MEC matrix elements. They are the sum of seagull (diagrams a,b), pion in flight (diagram c), and Δ (diagrams d–g) contributions

3. Results

In this section, we present the results for the effects of MEC on the 1p1h response functions using several models: the relativistic Fermi gas, the relativistic mean field, and the generalized SuSAM* model. By employing these different models, we take into account relativistic kinematics and we can analyze the impact of including the relativistic effective mass of the nucleon and the Δ resonance appearing in the MEC. The scaling analysis described in the previous Section allows us to study the influence of MEC on the generalized scaling function also in the region $|\psi^*| > 1$ where the RFG and RMF responses are zero. Moreover, we can investigate how the inclusion of MEC affects the scaling function and compare it with the predictions of the RFG and RMF models.

Unless stated otherwise, we present the results for ^{12}C with a Fermi momentum of $k_F = 225 \text{ MeV}/c$. We use an effective mass of $M^* = 0.8$, following the same choice of parameters as in References [56,57]. The calculation of 1p1h responses involves evaluating the 1p1h matrix element of the MEC, as given by Equation (15). This requires performing a numerical three-dimensional integration to account for the momentum dependence. Subsequently, a one-dimensional integration is carried out to calculate the averaged single-nucleon responses, as described in Equation (31).

First, since this work is an extension of the MEC model from Ref. [62] to the superscaling formalism, we compare it with the OB-MEC interference responses presented in [62] within the framework of the RFG. It should be noted that in [62] a different version of the Δ current was used. The Δ current was obtained from the $\gamma N\Delta$ Lagrangian proposed by Pascalutsa [78]

$$\mathcal{L}_{\gamma N\Delta} = ie \frac{G_1}{2m_N} \bar{\psi}^\alpha \Theta_{\alpha\mu} \gamma_\nu \gamma_5 T_3^\dagger N F^{\nu\mu} + \text{h.c.}, \quad (61)$$

plus $O(1/m_N^2)$ terms that give negligible contribution in the quasielastic energy region. The tensor $\Theta_{\alpha\mu}$ may contain an off-shell parameter and another arbitrary parameter related to the contact invariance of the Lagrangian. In this work, we use the simplest form

$$\Theta_{\alpha\mu} = g_{\alpha\mu} - \frac{1}{4} \gamma_\alpha \gamma_\mu. \quad (62)$$

The coupling constant G_1 was determined in [78] by fitting Compton scattering on the nucleon. However, there is a detail that needs to be clarified: the isospin operator used by Pascalutsa is normalized differently from the standard convention. That is, $T_i^{\text{Pascalutsa}} = \sqrt{\frac{3}{2}} T_i$, where T_i is the operator used in our calculation. This means that if we use the standard T_i in the Lagrangian (61), it should be multiplied by $\sqrt{\frac{3}{2}}$. This is equivalent to multiplying Pascalutsa's coupling constant $G_1 = 4.2$ by the factor $\sqrt{\frac{3}{2}}$. In Reference [62], this detail went unnoticed, and the $\sqrt{3/2}$ factor was not included in the calculations.

Using the Lagrangian given by Equation (61), the following Δ current is obtained:

$$j_{\Delta F}^\mu = [(T_i T_3^\dagger) \otimes \tau_i]_{t_1' t_2', t_1 t_2} \frac{f f^*}{m_\pi^2} F_\Delta(Q^2) V_{\pi NN}^{s_2' s_2}(p_2', p_2) F_{\pi N\Delta}(k_2^2) \bar{u}_{s_1'}(p_1') k_2^\alpha \left[\Theta^{\alpha\beta} G_{\beta\rho}(p_1 + Q) \frac{G_1}{2m_N} [\Theta^{\rho\mu} \gamma^\nu - \Theta^{\rho\nu} \gamma^\mu] \gamma_5 Q_\nu \right] u_{s_1}(p_1) + (1 \leftrightarrow 2) \quad (63)$$

and a similar expression for the Δ backward current. This current was used in Ref. [62] to compute the OB-MEC interference with the following form factor

$$F_\Delta(Q^2) = G_E^p(Q^2) \left(1 - \frac{Q^2}{3.5(\text{GeV}/c)^2} \right)^{-1/2} \quad (64)$$

where G_E^p is the electric form factor of the proton.

In Figure 3, we present the interference between the OB and Δ currents in the transverse response of ^{40}Ca . We compare our results with the model of Reference [62] in RFG, where the Lagrangian of Pascalutsa was used. The results of [62] were corrected with the factor of $\sqrt{\frac{3}{2}}$ mentioned earlier. For $q = 500 \text{ MeV}/c$, there is little difference between the two models. However, for $q = 1 \text{ GeV}/c$, the difference becomes more noticeable.

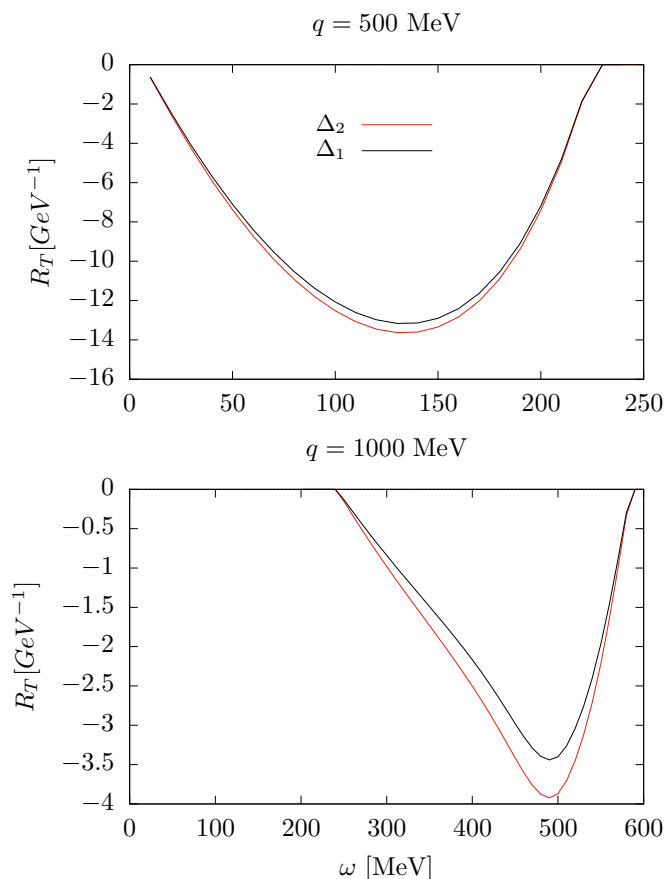


Figure 3. Interference OB-MEC in the transverse response of ^{40}Ca for two values of the momentum transfer, with $k_F = 237 \text{ MeV}/c$. In the graph, the curve labeled Δ_1 corresponds to using the Δ current of the present work in RFG. The curve Δ_2 corresponds to the calculation from Reference [62].

The results of Figure 3 show that the Δ current model used in this work does not differ significantly from the model in Reference [62], providing similar results. The small differences observed can be attributed to the different form factor and coupling constants, and can be understood as a model dependence in these results. From here on, all the results refer to the Δ current model described in the Equations (44) and (45).

It is expected that any relativistic model should reproduce the results of the well-established non-relativistic model for small values of energy and momentum in the non-relativistic limit [85]. As a check in this regard, in Figure 4, we compare the present model with the non-relativistic Fermi gas model from Ref. [15]. The non-relativistic Δ current used is taken from [62]. To perform this comparison, the same form factors and coupling constants are used in the relativistic and non-relativistic models. To take this limit in Figure 4, we follow the procedure as follows: q is small and $k_F = q/2$. We show the comparison between the two models for various values of q ranging from 100 to 500 MeV/c . In the left panels, we present the contribution of the transverse response stemming from the interference OB- π between the pure pionic MEC (diagrams a–c in Figure 2), and in the right panels, we show the OB- Δ interference (diagrams d–g in Figure 2) for the same values of q . As expected, we observe that for $q = 100 \text{ MeV}/c$, the relativistic and non-relativistic models practically coincide, demonstrating the consistency between the two models in the non-relativistic limit.

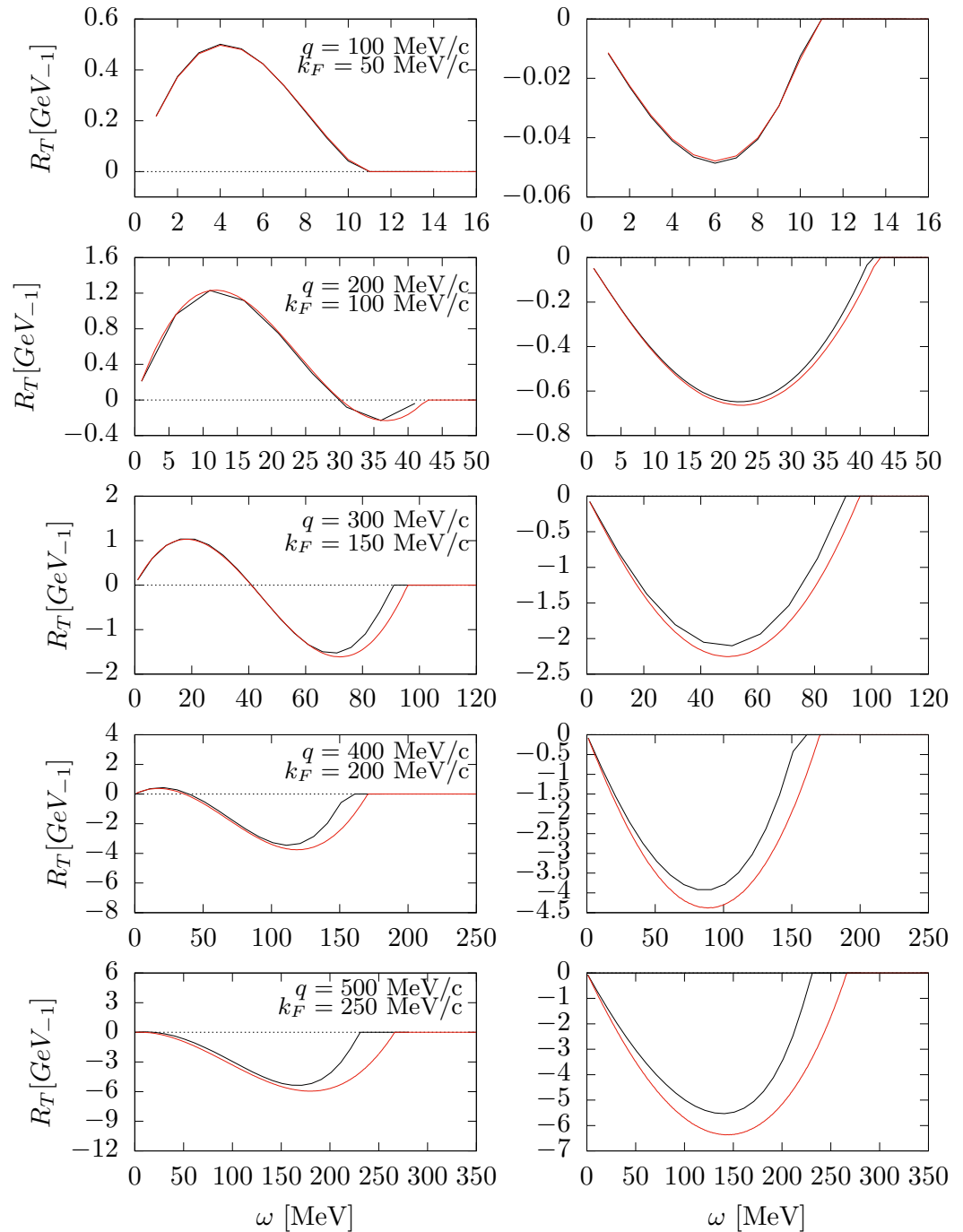


Figure 4. Comparison between relativistic and non-relativistic MEC transverse responses in ^{12}C . Black lines: RFG. Red lines: non-relativistic Fermi gas. Left panels show the interference OB- π , and left panels the interference OB- Δ . In these calculations the strong form factors in the pion vertices are set to one.

In Figure 4, one can also observe that for low values of q , the dominant contributions to the MEC are from the seagull and pion-in-flight diagrams, with the seagull diagram playing a particularly important role. These diagrams contribute positively to the MEC, enhancing the overall response. On the other hand, the contribution from the Δ resonance is negative. As q increases, the influence of the Δ resonance becomes more significant, and it starts to dominate the MEC contribution for q values around 400 MeV/c.

Before performing the scaling analysis, we examine the averaged single-nucleon responses that are used to scale the data. In Figure 5, we display the longitudinal and transverse single-nucleon responses for various values of q as a function of the scaling variable.

The calculated responses are shown separately for the OB current and the total responses including the MEC and taking into account the sum of protons and neutrons. The total response, which we define in Equation (36), comes from the product of the single nucleon with the phenomenological scaling function obtained from the (e, e') data as shown below. We used a Fermi distribution, Equation (37), with a smearing parameter $b = 50$ MeV/c, although the single-nucleon responses do not depend much on this specific value. It is observed that the effect of the MEC is negligible in the longitudinal response, as the curves for the OB current and total response overlap. However, in the transverse response, the effect of the MEC becomes appreciable, resulting in a reduction in the w_T response compared to the OB current. This reduction can be attributed to the interference between the one-body and two-body currents, which leads to a modified transverse response. The comparison between the OB current and the total response including the MEC provides insights into the contributions of the MEC to the single-nucleon responses and sets the stage for the subsequent scaling analysis.

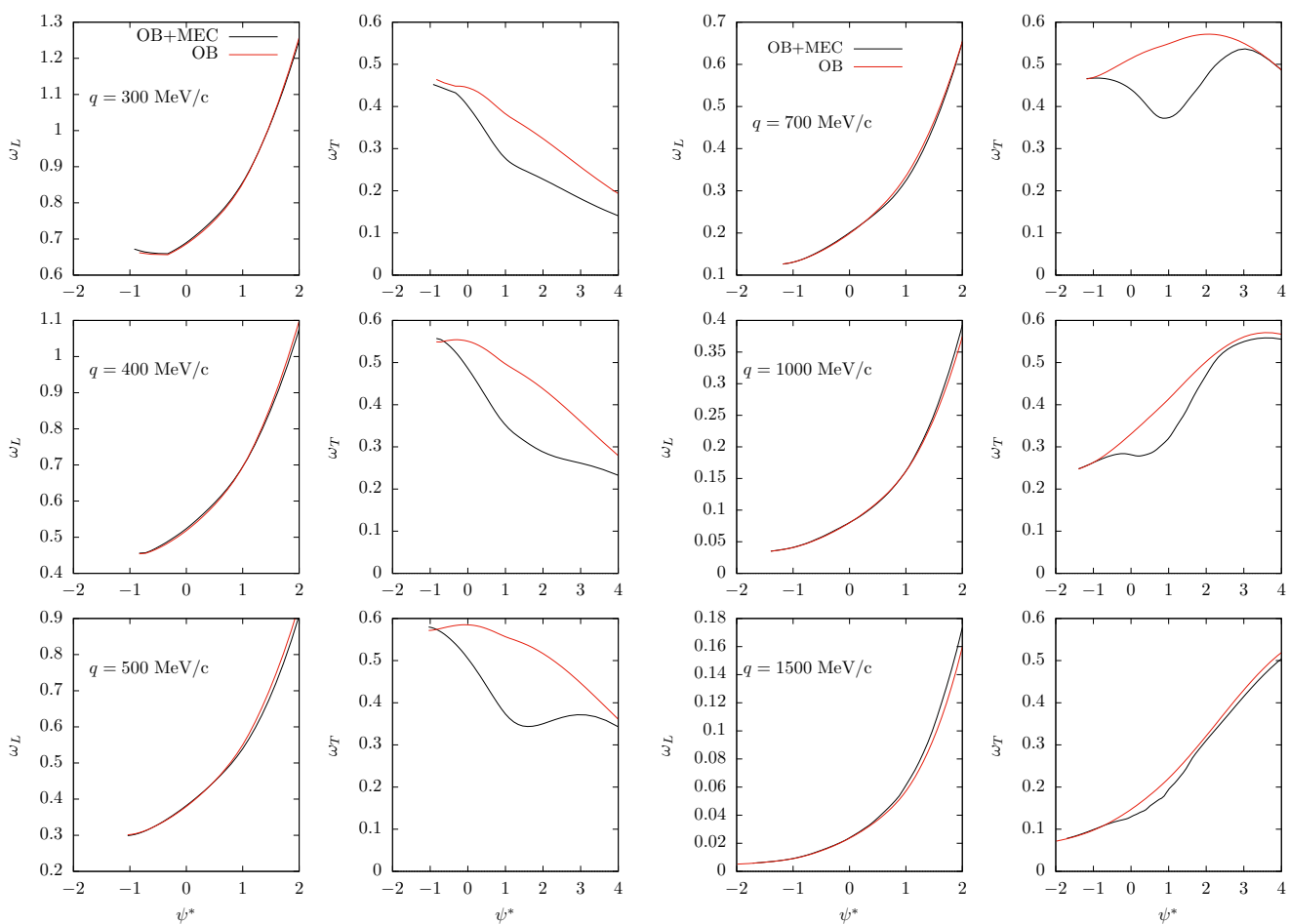


Figure 5. Averaged single-nucleon responses computed with and without MEC, for several values of the momentum transfer as a function of the scaling variable ψ^* .

Note that the center of the quasielastic peak corresponds to $\psi^* = 0$, where the energy and momentum can be transferred to a nucleon at rest. We see that MEC have a larger impact in the region $\psi^* > 0$, that is, the right-hand side of the peak, corresponding to higher energy transfers.

In Figure 6, we present the scaling analysis of the ^{12}C data. In the top panel, the experimental data, f_{exp}^* , are plotted against ψ^* in the interval $-2 < \psi^* < 2$. The experimental data are from Refs. [86,87] and cover a wide electron energy range, from 160 MeV up to 5.8 GeV. We observe a significant dispersion of many data points, indicating a wide range

of inelastic scattering events. However, we also notice that a portion of the data points cluster together and collapse into a thick band. These data points can be considered as associated to quasielastic (1p1h) events. To select these quasielastic data, we apply a density criterion. For each point, we count the number of points, n , within a neighborhood of radius $r = 0.1$, and eliminate the point if n is less than 25. Points that are disregarded are likely to correspond to inelastic excitations and low energy processes that violate scaling and cannot be considered within quasielastic processes. We observe that the remaining selected points, about half of the total, shown in the middle panel of Figure 6, form a distinct thick band. These points represent the ones that best describe the quasielastic region and approximately exhibit scaling behavior. The red curve represents the phenomenological quasielastic function $f^*(\psi^*)$ that provides the best fit to the selected data using a sum of two Gaussian functions:

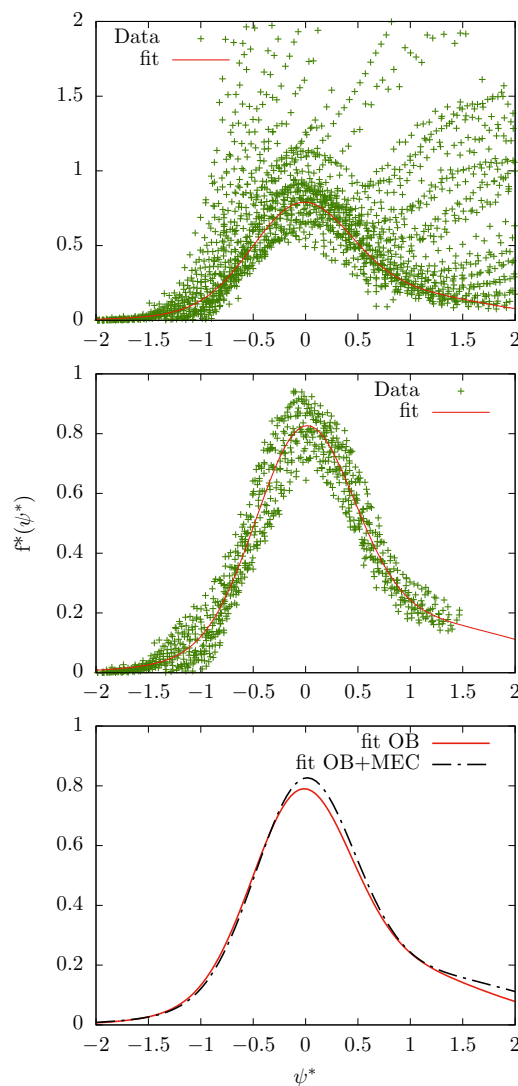


Figure 6. Scaling analysis of ^{12}C data including MEC and relativistic effective mass $M^* = 0.8$. The Fermi momentum is $k_F = 225$ MeV/c. In the top panel, we show the data points after scaling, representing the overall distribution. In the middle panel, we display the selected data points, which are chosen after eliminating those that do not exhibit clear scaling behavior. In the bottom panel, we present the phenomenological scaling function, which is fitted to the selected data points, compared to the scaling function obtained in a similar analysis without MEC. Experimental data are taken from Refs. [86,87].

$$f^*(\psi^*) = a_3 e^{-(\psi^* - a_1)^2 / (2a_2^2)} + b_3 e^{-(\psi^* - b_1)^2 / (2b_2^2)}. \quad (65)$$

The parameters found are shown in Table 1.

Table 1. Table of fitted parameters of the scaling function.

a_1	a_2	a_3	b_1	b_2	b_3
−0.01015	0.46499	0.69118	0.86952	1.16236	0.17921

In the bottom panel of Figure 6, we compare the scaling function obtained in our analysis with the scaling function obtained without including the MEC contributions. When including the MEC, the scaling function appears slightly higher since the single-nucleon response with MEC is slightly smaller than without them. However, both analyses provide a similarly acceptable description of the data. This suggests that while the MEC do have an impact, their effect is relatively small and does not significantly alter the overall scaling pattern observed in the data.

Upon examining the middle panel of Figure 6, we observe a significant variation within the band of selected points. This variation serves as a measure of scaling violation. In the vicinity of the peak, we note a variation of approximately 20%. However, as we move away from the QE peak, the scattering of data points exceeds 20%, reaching up to 100% at low omega. This scaling violation was first identified and extensively discussed in Reference [75], where a similar band was obtained without the inclusion of meson-exchange currents (MEC). It is worth noting that there are approximately 1500 data points comprising the QE band in the middle panel of Figure 6. This implies that a large set of data are close to the factorized formula in a first approximation within the peak region. However, outside the peak, the factorization describes the data less accurately. Scaling violation should be attributed to various nuclear processes that break the factorization of the cross-section into a single-nucleon response times a scaling function. These processes include final state interactions, Random Phase Approximation (RPA), nuclear correlations, finite-size effects, residual inelastic effects, and more. Additionally, these effects can have differing impacts on the transverse and longitudinal response, with their combined magnitude accounting for approximately 10% of the scaling violation at the peak. Notably, our analysis, when compared to previous studies [75], shows that the inclusion of MEC 1p1h effects has little to no effect on the amplitude of the scaling violation.

Now that we have obtained the phenomenological scaling function through the scaling analysis, we can utilize this function to calculate the response functions of the model beyond the RMF. By multiplying the scaling function by the averaged single-nucleon responses, as stated in Equation (36), we can extend our calculations to different kinematic regimes and explore the behavior of the responses beyond the relativistic mean field description. This allows us to investigate the influence of various factors, such as the MEC and relativistic effects, on the response functions and cross-sections.

In Figures 7–10, we present the interferences of the OB-MEC in the response functions for different values of q (500, 700, 1000, and 1500 MeV/c). We separate the interferences into OB-seagull, OB-pionic, and OB- Δ contributions for both the longitudinal and transverse responses as functions of ω . Each panel displays three curves corresponding to the free RFG (with effective mass $M^* = 1$), the RMF (with effective mass $M^* = 0.8$), and the present SuSAM* model. These figures allow us to analyze the relative contributions of the different OB-MEC interferences in the response functions at various kinematic regimes. By comparing the results obtained from the RFG, RMF, and SuSAM* models, we can observe the effects of including the relativistic interaction through the effective mass and the scaling function on the interferences.

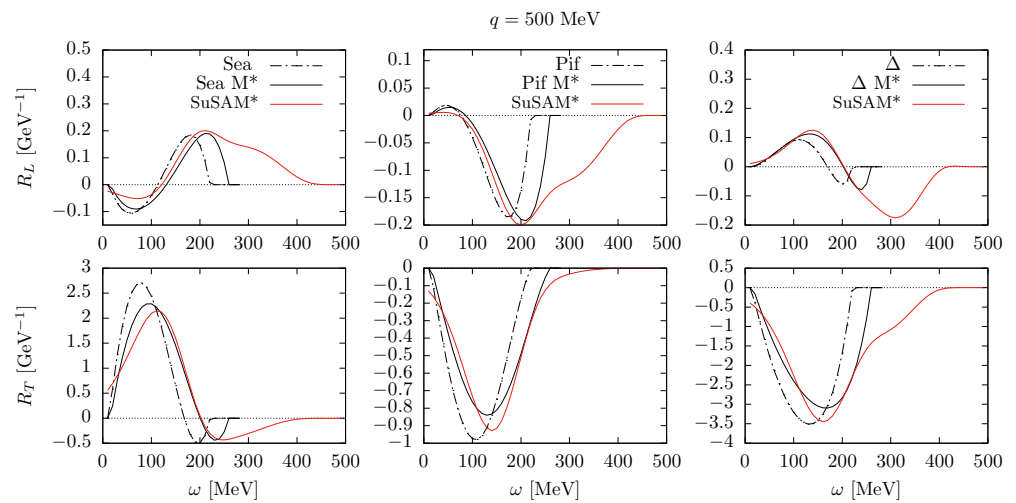


Figure 7. Interference OB-MEC responses separated in seagull, pion-in-flight, and Δ contributions for ^{12}C and $q = 500$ MeV/c. In each panel we compare the results of RFG (with $M^* = 1$, dot-dash), with the RMF (with $M^* = 0.8$) and the SuSAM* model.

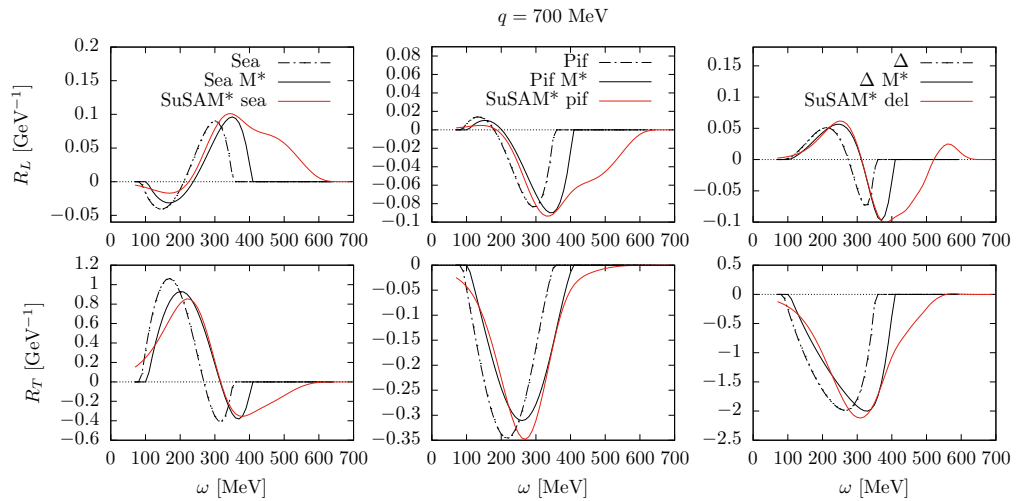


Figure 8. The same as Figure 7 for $q = 700$ MeV/c.

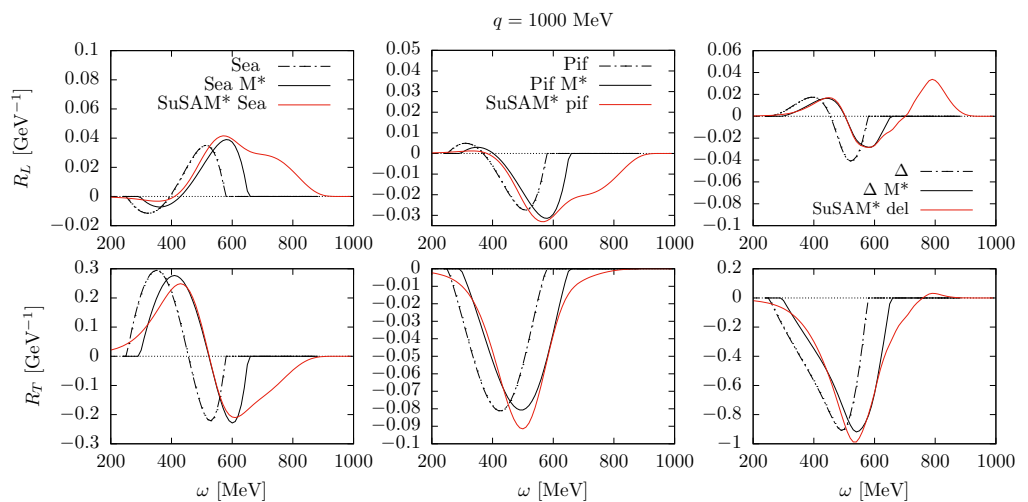


Figure 9. The same as Figure 7 for $q = 1000$ MeV/c.

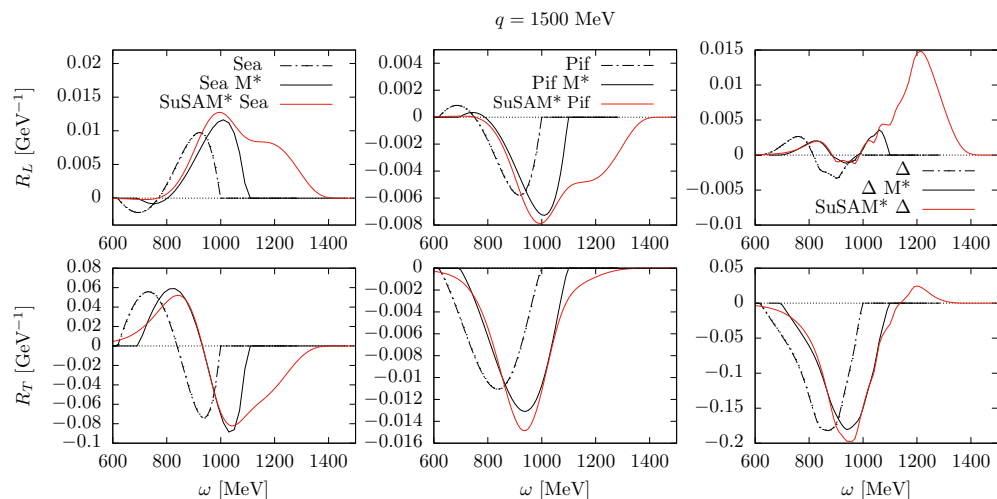


Figure 10. The same as Figure 7 for $q = 1500 \text{ MeV}/c$.

First we observe that the introduction of the effective mass $M^* = 0.8$ shifts the responses to the right, towards higher energy values. The effective mass takes into account the binding of the nucleon in the nucleus, which causes the quasielastic peak to approximately coincide with the maximum of the experimental cross-section. In the RFG, this is traditionally taken into account by subtracting a binding energy of approximately 20 MeV from ω to account for the average separation energy of the nucleons. In the RMF, this is automatically included by considering the effective mass of the nucleon, $M^* = 0.8$, which was adjusted for ^{12}C precisely to achieve this effect.

In the transition from the RMF to the SuSAM* model, we replace the scaling function of the RFG with the phenomenological scaling function that we adjusted. This new scaling function extends beyond the region of $-1 < \psi^* < 1$, where the RFG scaling function is zero. As a result, we observe in Figures 7–10 that the interferences acquire a tail towards high energies, similar to the behavior of the scaling function.

The tail effect is more pronounced in the longitudinal responses because the single-nucleon longitudinal response, as shown in Figure 5, increases with ω . This amplifies the tail when multiplied by the scaling function. However, it is important to note that the contribution of the MEC to the longitudinal response is relatively small compared to the dominant transverse response. Therefore, while the tail effect is observed in the longitudinal responses, its impact on the cross-section is not as significant as in the transverse channel, if not negligible.

In the dominant transverse response, the seagull contribution from the MEC is positive, leading to an enhancement of the response, while the pionic and Δ contributions are negative, causing a reduction in the overall response when including the MEC. This is in line with pioneering calculations by Kohno and Otsuka [63] and by Alberico et al. [64] in the non-relativistic Fermi gas. Moreover, in shell model calculations, similar results have been obtained [15], showing that the MEC contributions also lead to a tail and extension of the response functions to higher values of ω , as in the SuSAM* approach. It is worth noting that the relative importance of these contributions can depend on the momentum transfer q and the energy transfer ω . For the values considered in Figures 7–11, the Δ current is found to be the dominant contribution, leading to a net negative effect from the MEC.

The observation in Figure 10 of a sign change and a small bump in the OB- Δ transverse response for high values of ω is indeed interesting. The change of sign is already observed for $q = 1 \text{ GeV}/c$ in Figure 9. This connects with the findings in Reference [16], where a pronounced bump and sign change were reported in a semi-relativistic shell model calculation based on the Dirac equation with a relativistic energy-dependent potential. In the present calculation, the bump is observed but it is very small compared to the results of Ref. [16]. It is important to note that, in the present work, the fully relativistic SuSAM* approach is employed, which takes into account the dynamical properties of both nucleons

and the Δ , as well as the scaling function. This differs from the approach in Reference [16], where a static propagator for the Δ was used. To definitively clarify the difference with the present results, a fully relativistic calculation in finite nuclei, considering the dynamical properties of the Δ would be necessary.

The comparison of the OB-MEC interference with the MEC contribution alone (represented by $w_{12}^{\mu\nu}$ and $w_2^{\mu\nu}$, respectively, in Equation (21)) in the transverse response is shown in Figures 11 and 12. We observe that the MEC contribution alone represents a small and almost negligible contribution to the transverse response. This justifies the previous calculations that focused only on the OB-MEC interference (e.g., the semi-analytical calculations in References [15,88] for the non-relativistic Fermi gas), as it provides an excellent approximation. This observation holds true for both the RMF model in Figure 11 and the SuSAM* model in Figure 12. It highlights the fact that the dominant contribution to the transverse response arises from the interference between the OB and MEC, while the pure MEC contribution is relatively small. It is also worth stressing that while the pure MEC contribution is, of course, positive, the interference contribution is negative.

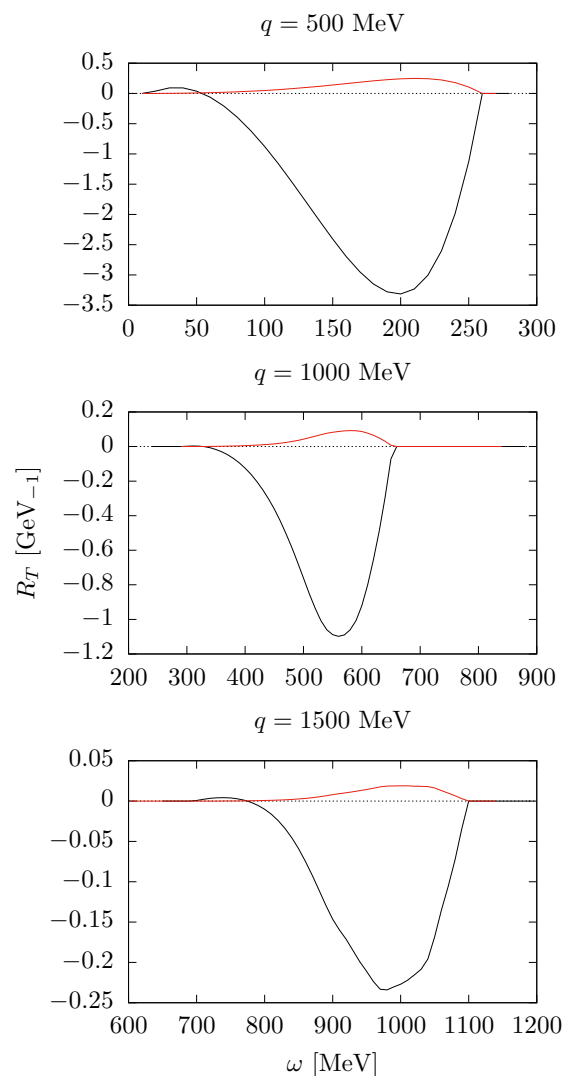


Figure 11. Comparison of OB-MEC interference in the transverse response (black lines) with the pure MEC transverse response (red lines) for several values of q in the RMF model.

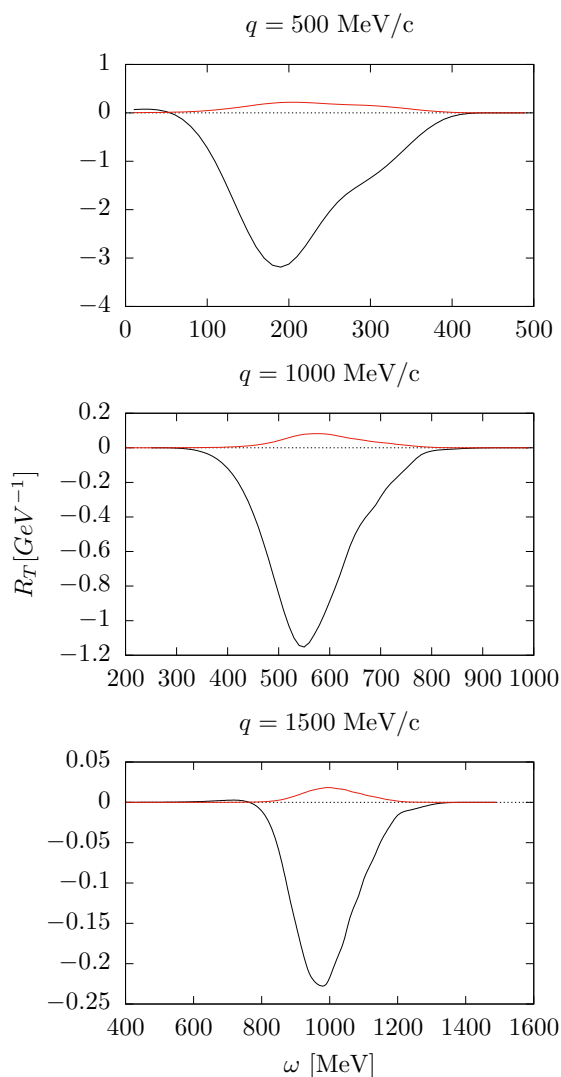


Figure 12. The same as Figure 11 in the SuSAM* model.

In Figure 13, we present the total responses of ^{12}C computed using the generalized SuSAM* model. These responses are obtained by multiplying the phenomenological scaling function by the averaged single-nucleon response and summing over protons and neutrons, as given by Equation (36). The responses are shown for different values of q as a function of ω . In the same figure, we also show the results without including the MEC contributions, which corresponds to setting the terms $w_{12} + w_2$ associated with the two-body current (Equation (21)) to zero.

Comparing the results with and without MEC, we observe that the impact of MEC is more significant in the transverse response compared to the longitudinal response. This is expected since the corrections due to MEC in the longitudinal response are higher-order effects in a non-relativistic expansion in powers of v/c , as known from previous studies [89]. Therefore, the MEC contributions to the longitudinal response are minimal and only start to become noticeable for $q > 1$ GeV in the high-energy region. However, this high-energy region is dominated and overshadowed by pion emission and inelastic processes, making it difficult to isolate the 1p1h longitudinal response.

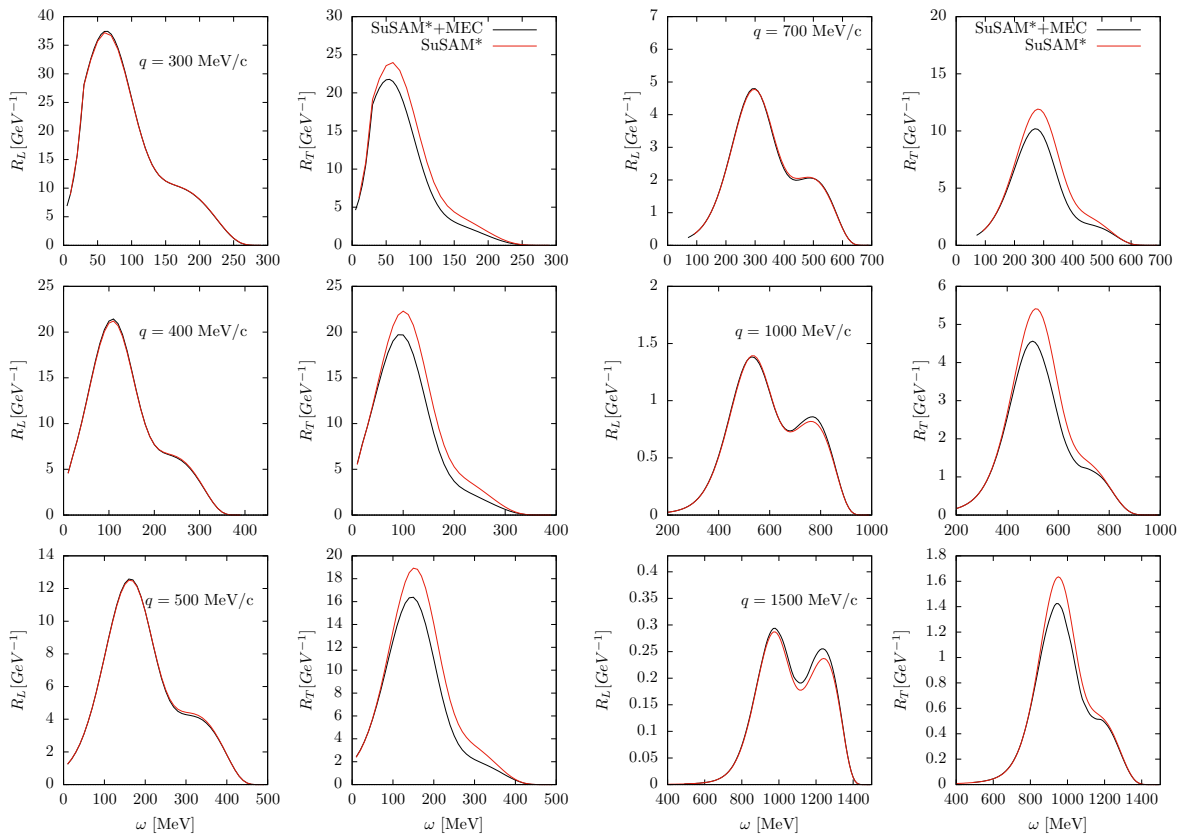


Figure 13. Response functions calculated in the generalized SuSAM* model (black curves). The red curves do not include the MEC.

The inclusion of MEC in the single nucleon leads to a reduction in the transverse response by around 10% or even more for all studied values of q . This is consistent with previous calculations in RFG and the shell model [14–16,62,90]. These calculations have consistently shown that MEC in the $1p1h$ channel tend to decrease the transverse response compared to the contribution from the one-body current. It is important to note that this reduction in the transverse response is a direct consequence of the destructive interference between the one-body current and MEC. The contribution of MEC to the transverse response is negative because the direct two-body matrix element is zero (in symmetric nuclear matter, $N = Z$) or almost zero (in asymmetric nuclear matter, $N \neq Z$, or in finite nuclei) after summing over isospin.

The treatment of the Δ resonance in the medium is subject to various ambiguities and uncertainties. In our generalized SuSAM* model, we assume that the Δ resonance acquires an effective mass M_{Δ}^* and vector energy E_{ν}^{Δ} due to its interaction with the RMF. This requires modifying the propagator according to the formalism proposed in References [41,84]. To estimate the effect of this treatment, in Figure 14 we compare the transverse response for the OB- Δ interference calculated assuming that the Δ remains unchanged in the medium, i.e., setting $M_{\Delta}^* = M_{\Delta}$ and $E_{\nu}^{\Delta} = 0$. The response with the free Δ without medium modifications is slightly smaller in absolute value, around 10% depending on the momentum transfer. This can be seen as an estimation of the uncertainty associated with the Δ interaction in the medium.

Another related issue is the modification of the Δ width in the medium, which we have not considered here assuming the free width (59). This effect can also influence the results, but it is expected to be of the same order as the observed effect in Figure 14. It is important to note that the treatment of the Δ resonance in the medium is a complex topic, and further investigations and refinements are needed to fully understand its effects and uncertainties.

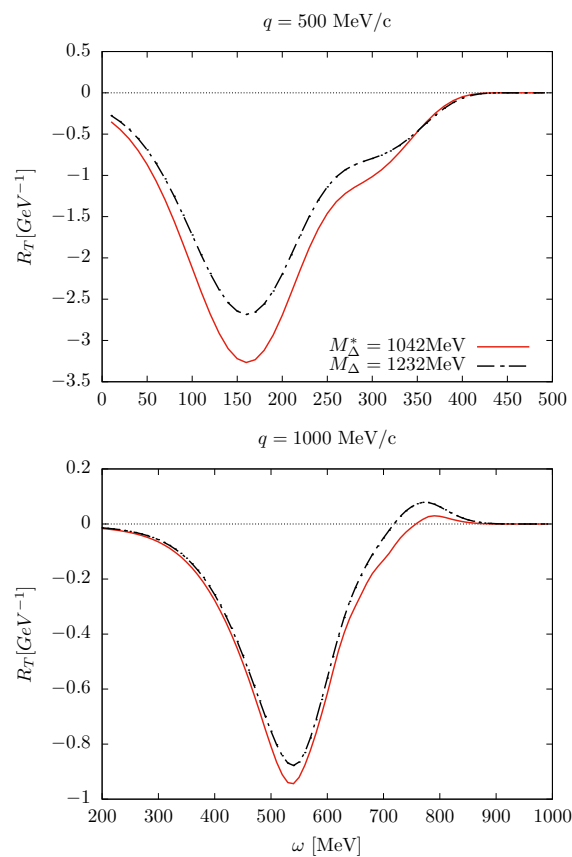


Figure 14. Comparison of the transverse interference OB- Δ computed in the generalized SuSAM* model with and without relativistic effective mass and vector energy for the Δ .

In Figure 15, we compare the total transverse response calculated in the RMF model with an effective mass of $M^* = 0.8$ to the results obtained in the generalized SuSAM* approach for various momentum transfers, ranging from $q = 300$ MeV/c to $q = 1500$ MeV/c. Both calculations include the effects of MEC. One notable difference between the two approaches is the presence of a pronounced tail at high energy transfer rates in the SuSAM* results. This tail extends well beyond the upper limit of the RFG responses, reflecting the effect of the phenomenological scaling function used in the SuSAM* approach. Similar effects are found in the longitudinal response. Additionally, it is worth noting that the peak height of the transverse response in the SuSAM* approach is generally higher compared to the RMF model. Overall, the comparison in Figure 15 highlights the improvements and additional physics captured by the SuSAM* approach, by extending the scaling function of the RFG to describe the transverse response in a wider energy transfer range.

Finally, in Figure 16, we present the results for the (e, e') double differential cross-section of ^{12}C calculated with the generalized SuSAM* model including MEC, compared to experimental data for selected kinematics. We also compare these with the same model but assuming that only the single-nucleon contribution is present, i.e., setting the MEC to zero. We observe that the inclusion of MEC in this model leads to a small reduction in the cross-section compared to the case without MEC. This reduction is a consequence of the decrease in the transverse response due to the presence of MEC.

Figure 16 also provides an illustrative example of the averaged description of the global (e, e') cross-section data. It is important to note that considering the scaling violation uncertainty—the scatter of the points in the scaling band is larger than 20%—significant deviations from the QE data are expected for certain kinematic conditions. In some cases, the predicted cross-section is above the data, while in others, it is below. It is important to note that the phenomenological scaling function is derived by excluding data points that significantly deviate from scaling behavior. Specifically, kinematics involving substantial contributions from pion emission are excluded as non-quasielastic. Consequently, in these

cases, the predicted cross-section falls below the experimental data. A more comprehensive and detailed comparison is available in Refs. [19,70], where results are presented using a phenomenological scaling band for a broader range of kinematics. We refer interested readers to that reference since the results for the cross-section do not differ significantly from those presented therein. This similarity arises because, while we incorporate MEC within the single-nucleon framework in this work, the new scaling analysis primarily shifts the data points slightly with respect to the one-body current case, thus modifying the scaling function band only marginally. The description of the cross-section, however, remains practically the same.

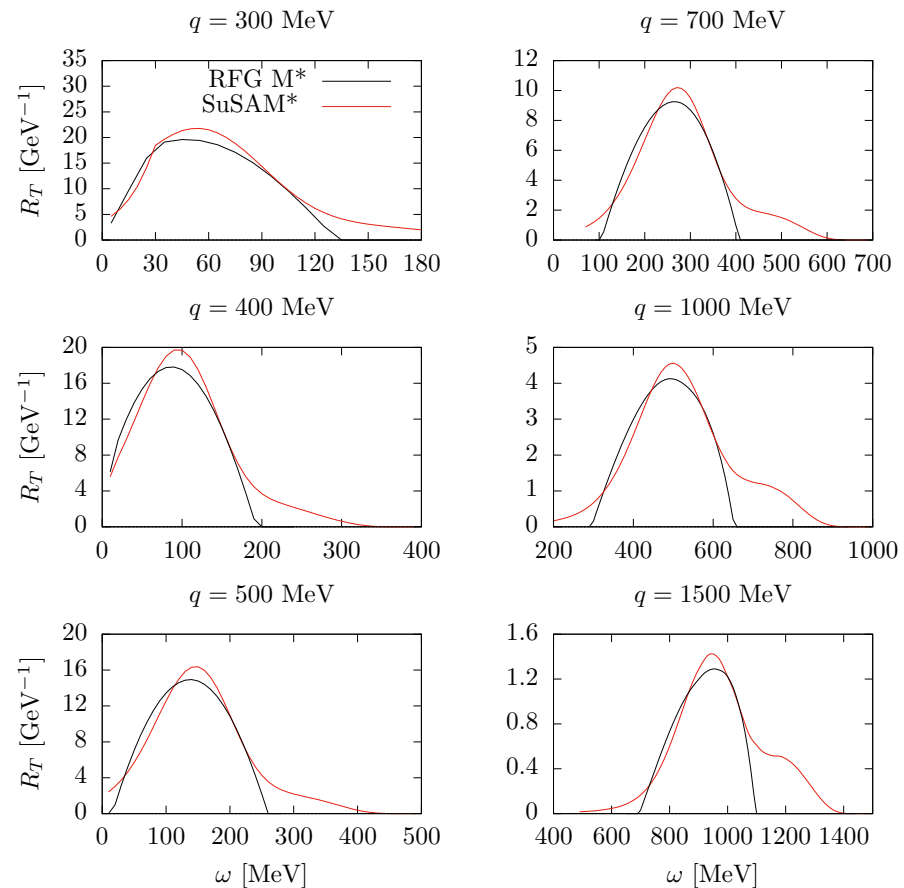


Figure 15. Total transverse responses for ^{12}C including MEC in the RMF model with $M^* = 0.8$ compared to the generalized SuSAM* model.

This work does not include comparisons with separate response function data or the Coulomb sum rule. While the scaling band results from the clustering of data points with varying momentum and energy transfers, the faithful reproduction of separate response functions by a model is not necessarily guaranteed. To ensure the accuracy of a scaling-based approach in describing response functions, it would be imperative to somehow incorporate experimental information about these response functions into the scaling analysis. This is an endeavor that requires further investigation beyond the scope of this study, which primarily serves to illustrate how to modify the scaling approach to incorporate MEC within the single-nucleon framework.

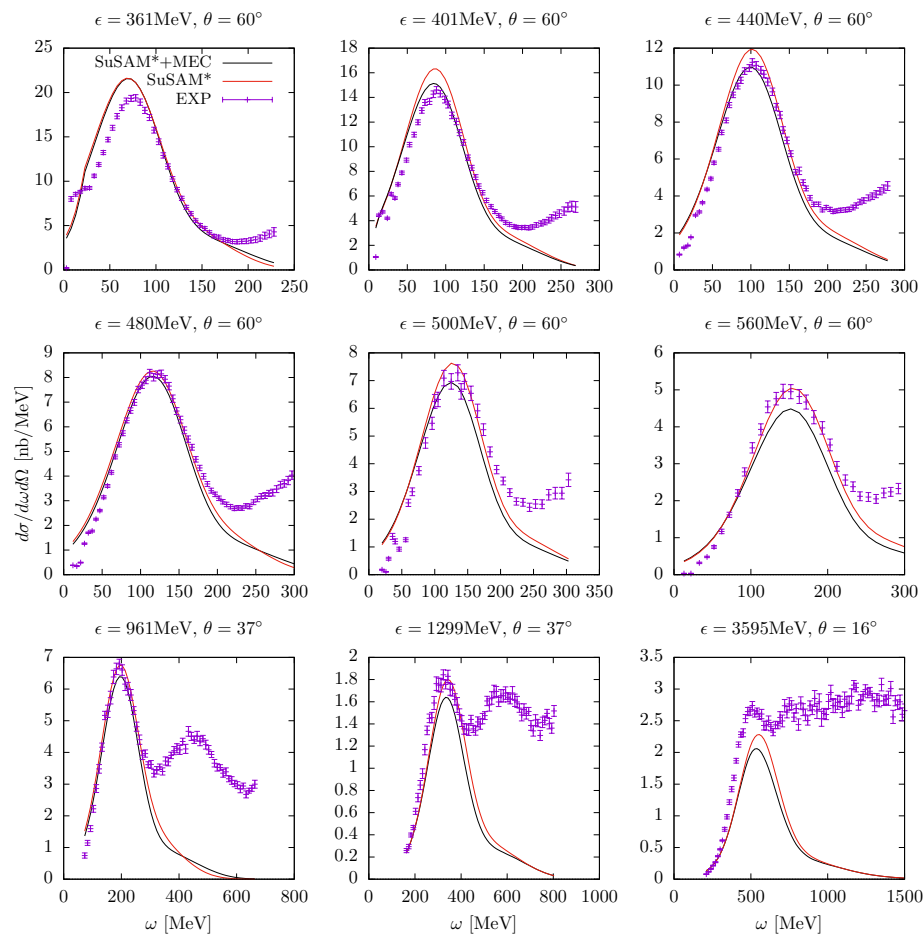


Figure 16. Cross-section of ^{12}C for several kinematics computed with the generalized SuSAM* model, including MEC, compared with the same calculation without MEC. Experimental data are from Refs. [86,87].

4. Discussion and Concluding Remarks

From the results seen in the previous section, we observe that, in all the models considered, the transverse response decreases when including meson-exchange currents in the $1p1h$ channel. This result is consistent with previous independent calculations performed in the relativistic and non-relativistic Fermi gas models as well as in the non-relativistic and semi-relativistic shell models. The result is a consequence of the fact that the main contribution arises from the interference of the OB and Δ currents, in particular through the exchange diagram, carrying a minus sign. The contribution from the direct part of the MEC matrix element is zero in the Fermi gas, and this is the reason for the negative contribution.

It is worth mentioning the existence of some calculations that disagree with this result and suggest a different effect of MEC on the transverse response. We would like to comment in particular on two notable model calculations: the Green Function Monte Carlo (GFMC) model from Reference [11] and the Correlated Basis Function (CBF) calculation by Fabrocini [14], both including meson-exchange currents in the $1p1h$ sector. In both approaches, the effect of MEC is positive in the quasielastic peak and quite significant, around 20%, in the transverse response. This substantial effect is attributed to the simultaneous effect of tensor correlations in the wave function and MEC. In fact, in Fabrocini's calculation, the origin of this effect was found to be the tensor-isospin correlation contribution in the direct matrix element of the Δ current, which is non-zero when summing over isospin for correlated wave functions. This effect can also be understood in terms of the presence of short-range correlations in the nuclear wave function. The direct matrix element of MEC, when a proton is emitted, involves the interaction of the proton with protons as well as with

neutrons, i.e., the MEC matrix element involves PN and PP pairs. The high-momentum component of these pairs is significantly different because PN pairs contain the 3S_1 and 3D_1 deuteron-like waves, while PP pairs do not. Therefore, when summing over isospin, there is no cancellation between PP and PN pairs in the high-momentum part of the wave function, resulting in a non-zero direct matrix element. This is in agreement with the conclusion of Fabrocini, as the tensor-isospin term precisely generates this significant difference between PP and PN pairs. An alternative way to investigate this hypothesis would be to perform calculations in the independent particle model by solving the Bethe–Goldstone equation [91] for PP and PN pairs and using a correlation current similar to the one proposed in [92]. Such calculations could provide further insights into the effect of short-range correlations on the MEC contributions to the transverse response.

On the other hand, the results of Fabrocini reproduce the well-known effect that MEC has a negative impact on the transverse response when the correlation's functions are set to zero, consistent with the results from uncorrelated models. Since in the present work we started with an uncorrelated model, the relativistic mean field, the effects of correlations in the transverse current are expected to be included phenomenologically in the scaling function. This and other mechanisms, such as final state interactions, contribute to the violation of scaling observed in the data.

In conclusion, this work presents a method that enables the consistent inclusion of meson-exchange currents (MEC) within the framework of the superscaling analysis with relativistic effective mass. The approach is rigorously relativistic, drawing its foundation from the relativistic mean field theory of nuclear matter. The generalized scaling analysis is comprehensively illustrated and applied to the (e,e') cross-section of ${}^{12}\text{C}$. To achieve this, we introduce a novel definition of the single-nucleon tensor within the model's factorization. The averaged single-nucleon hadronic tensor is defined by the summation of one-body and two-body currents, with no alteration to the definition of the scaling function, which retains its form as in the one-body current case within the Fermi gas. This averaging definition is extended beyond the scaling region of $-1 < \psi^* < 1$ characteristic of the Fermi gas, achieved by slightly modifying the momentum distribution through a smeared Fermi distribution. This adaptation allows for the evaluation of MEC for any value of the scaling variable.

Through the inclusion of MEC and the utilization of a phenomenological scaling function, we conducted a comparative analysis of the $1p1h$ response functions within the context of the RFG, RMF, and SuSAM* models. In these models, MEC diminish the transverse response, while the longitudinal response remains relatively unaffected by their presence. This observation aligns with previous calculations in other independent particle models, most notably within shell model calculations [15,16]. Our detailed examination of the interference responses between one- and two-body currents sheds light on the influence of the effective mass, resulting in a rightward shift and slight modifications in strength. As an essential test of the results, we verified that in the low-momentum limit, the predictions of the relativistic model align with those of the non-relativistic model in the Fermi gas.

The generalized scaling analysis, augmented with the inclusion of MEC, offers a global description of the quasielastic electron cross-section, albeit solely as an average representation. The selected QE data generate a band with scatter of $\sim 20\%$ at the maximum, highlighting the extent of scaling violation. By design, this approach is not intended for precise cross-section calculations. When the effect of MEC is incorporated within the single-nucleon framework, the scaling data undergo only slight modifications, well within a percentage considerably smaller than the uncertainty within the scaling band. Consequently, the overall description of the cross-section is minimally impacted by the inclusion of MEC, relative to the use of the OB current alone.

We anticipate that the landscape may undergo transformation with the development of a more realistic averaged single-nucleon framework, possibly incorporating a Fermi gas description enhanced by short-range correlations. In such a scenario, the meson-exchange currents (MEC) are expected to exert a more substantial influence, potentially leading to

a significant increase in the transverse response. This paper demonstrates, for the first time, the methodology for incorporating these modifications within the SuSAM* formalism, highlighting its significance.

A central question remains as to whether it is feasible to identify more realistic single-nucleon responses capable of diminishing the degree of scaling violation within the scaling data. If successful, such a model could offer enhanced predictive capabilities. Alternatively, exploring variations in the single-nucleon responses, akin to a phenomenological parametrization in both the longitudinal and transverse channels, as exemplified by the Bodek–Christy model [12,13], remains a promising avenue for future investigation, including the extension of the model to study neutrino-nucleus scattering.

Author Contributions: All authors contributed to the conceptualization, methodology, software, validation, investigation, and writing. All authors have read and agreed to the published version of the manuscript.

Funding: This work is supported by: Grant PID2020-114767GB-I00 funded by MCIN/AEI /10.13039/501100011033; FEDER/Junta de Andalucía-Consejería de Transformación Económica, Industria, Conocimiento y Universidades/A-FQM-390-UGR20; Junta de Andalucía (Grant No. FQM-225); INFN under Project NUCSYS; and University of Turin under Project BARM-RILO-23-01.

Data Availability Statement: The cross-section datasets analyzed are available at Refs. [86,87].

Conflicts of Interest: The authors declare no conflict of interest.

Abbreviations

The following abbreviations are used in this manuscript:

OB	One-body
MEC	Meson-exchange currents
RFG	Relativistic Fermi gas
RMF	Relativistic mean field
SuSA	Superscaling analysis
SuSAM*	Superscaling analysis with relativistic effective mass

References

- Jourdan, J. Longitudinal response functions: The Coulomb sum revisited. *Phys. Lett. B* **1995**, *353*, 189–195. [[CrossRef](#)]
- Jourdan, J. Quasi-elastic response functions. The Coulomb sum revisited. *Nucl. Phys. A* **1996**, *603*, 117. [[CrossRef](#)]
- Fabrocini, A.; Fantoni, S. Microscopic calculation of the longitudinal response of nuclear matter. *Nucl. Phys. A* **1989**, *503*, 375. [[CrossRef](#)]
- Mihaila, B.; Heisenberg, J. Microscopic Calculation of the Inclusive Electron Scattering Structure Function in O 16. *Phys. Rev. Lett.* **2000**, *84*, 1403. [[CrossRef](#)]
- Sobczyk, J.E.; Acharya, B.; Bacca, S.; Hagen, G. Coulomb sum rule for He 4 and O 16 from coupled-cluster theory. *Phys. Rev. C* **2020**, *102*, 064312. [[CrossRef](#)]
- Carlson, J.; Schiavilla, R. Euclidean proton response in light nuclei. *Phys. Rev. Lett.* **1991**, *68*, 3682. [[CrossRef](#)]
- Carlson, J.; Jourdan, J.; Schiavilla, R.; Sick, I. Longitudinal and transverse quasielastic response functions of light nuclei. *Phys. Rev. C* **2002**, *65*, 024002. [[CrossRef](#)]
- Lovato, A.; Carlson, J.; Gandolfi, S.; Rocco, N.; Schiavilla, R. Ab Initio Study of (ν_l, l^-) , and $(\bar{\nu}_l, l^+)$ Inclusive Scattering in C 12: Confronting the MiniBooNE and T2K CCQE Data. *Phys. Rev. X* **2020**, *10*, 031068.
- Carlson, J.; Gandolfi, S.; Pederiva, F.; Pieper, S.C.; Schiavilla, R.; Schmidt, K.E.; Wiringa, R.B. Quantum Monte Carlo methods for nuclear physics. *Rev. Mod. Phys.* **2015**, *87*, 1067. [[CrossRef](#)]
- Lovato, A.; Gandolfi, S.; Carlson, J.; Pieper, S.C.; Schiavilla, R. Electromagnetic and neutral-weak response functions of ^4He and ^{12}C . *Phys. Rev. C* **2015**, *91*, 062501. [[CrossRef](#)]
- Lovato, A.; Gandolfi, S.; Carlson, J.; Pieper, S.C.; Schiavilla, R. Electromagnetic response of ^{12}C : A first-principles calculation. *Phys. Rev. Lett.* **2016**, *117*, 082501. [[CrossRef](#)] [[PubMed](#)]
- Bodek, A.; Christy, M.E. Extraction of the Coulomb sum rule, transverse enhancement, and longitudinal quenching from an analysis of all available $e-^{12}\text{C}$ and $e-^{16}\text{O}$ cross section data. *Phys. Rev. C* **2022**, *106*, L061305. [[CrossRef](#)]
- Bodek, A.; Christ, M.E. Contribution of nuclear excitation electromagnetic form factors in C 12 and O 16 to the Coulomb sum rule. *Phys. Rev. C* **2023**, *107*, 054309. [[CrossRef](#)]
- Fabrocini, A. Inclusive transverse response of nuclear matter. *Phys. Rev. C* **1997**, *55*, 338. [[CrossRef](#)]

15. Amaro, J.E.; Lallena, A.M.; Co, G. Meson exchange currents in quasielastic electron scattering from C-12 and Ca-40 nuclei. *Nucl. Phys. A* **1994**, *578*, 365–396. [[CrossRef](#)]
16. Amaro, J.E.; Barbaro, M.B.; Caballero, J.A.; Donnelly, T.W.; Maieron, C.; Udias, J.M. Meson-exchange currents and final-state interactions in quasielastic electron scattering at high momentum transfers. *Phys. Rev. C* **2010**, *81*, 014606. [[CrossRef](#)]
17. Rocco, N.; Lovato, A.; Benhar, O. Comparison of the electromagnetic responses of ^{12}C obtained from the Green's function Monte Carlo and spectral function approaches. *Phys. Rev. C* **2016**, *94*, 065501. [[CrossRef](#)]
18. Megias, G.D.; Amaro, J.E.; Barbaro, M.B.; Caballero, J.A.; Donnelly, T.W. Inclusive electron scattering within the SuSAv2 meson-exchange current approach. *Phys. Rev. D* **2016**, *94*, 013012. [[CrossRef](#)]
19. Amaro, J.E.; Ruiz Arriola, E.; Ruiz Simo, I. Superscaling analysis of quasielastic electron scattering with relativistic effective mass. *Phys. Rev. D* **2017**, *95*, 076009. [[CrossRef](#)]
20. Donnelly, T.W.; Jeschonnek, S.; Van Orden, J.W. General tensor structure for electron scattering in terms of invariant responses. *Annals Phys.* **2023**, *448*, 169174. [[CrossRef](#)]
21. Donnelly, T.W. High-Energy Lepton Scattering and Nuclear Structure Issues. *Universe* **2023**, *9*, 196. [[CrossRef](#)]
22. Fukuda, Y.; Hayakawa, T.; Ichihara, E.; Inoue, K.; Ishihara, K.; Ishino, H.; Itow, Y.; Kajita, T.; Kameda, J.; Kasuga, S.; et al. [Super-Kamiokande]. Evidence for oscillation of atmospheric neutrinos. *Phys. Rev. Lett.* **1998**, *81*, 1562. [[CrossRef](#)]
23. Adamson, P.; Ader, C.; Andrews, M.; Anfimov, N.; Anghel, I.; Arms, K.; Arrieta-Diaz, E.; Aurisano, A.; Ayres, D.S.; Backhouse, C. et al. [NOvA]. First measurement of electron neutrino appearance in NOvA. *Phys. Rev. Lett.* **2016**, *116*, 151806. [[CrossRef](#)]
24. MiniBooNE Collaboration; Aguilar-Arevalo, A.A.; Brown, B.C.; Bugel, L.; Cheng, G.; Conrad, J.M.; Cooper, R.L.; Dharmapalan, R.; Diaz, A.; Djurcic, Z.; et al. Significant excess of electronlike events in the MiniBooNE short-baseline neutrino experiment. *Phys. Rev. D* **2010**, *81*, 092005. [[CrossRef](#)]
25. Abe, K.; Amey, J.; Andreopoulos, C.; Anthony, L.; Antonova, M.; Aoki, S.; Ariga, A.; Ashida, Y.; Azuma, Y.; Ban, S.; et al. Characterization of nuclear effects in muon-neutrino scattering on hydrocarbon with a measurement of final-state kinematics and correlations in charged-current pionless interactions at T2K. *Phys. Rev. D* **2018**, *98*. [[CrossRef](#)]
26. Acciarri, R.; Adams, C.; Asaadi, J.; Baller, B.; Bolton, T.; Bromberg, C.; Cavanna, F.; Church, E.; Edmunds, D.; Ereditato, A.; et al. Measurements of inclusive muon neutrino and antineutrino charged current differential cross sections on argon in the NuMI antineutrino beam. *Phys. Rev. D* **2014**, *89*. [[CrossRef](#)]
27. Acero, M.A.; Adamson, P.; Aliaga, L.; Alion, T.; Allakhverdian, V.; Altakarli, S.; Anfimov, N.; Antoshkin, A.; Aurisano, A.; Back, A.; et al. First measurement of neutrino oscillation parameters using neutrinos and antineutrinos by NOvA. *Phys. Rev. Lett.* **2019**, *123*, 151803. [[CrossRef](#)]
28. Alvarez-Ruso, L.; Hayato, Y.; Nieves, J. Progress and open questions in the physics of neutrino cross sections at intermediate energies. *New J. Phys.* **2014**, *16*, 075015. [[CrossRef](#)]
29. Mosel, U. Progress and open questions in the physics of neutrino cross sections at intermediate energies. *Ann. Rev. Nuc. Part. Sci.* **2016**, *66*, 171. [[CrossRef](#)]
30. Katori, T.; Martini, M. Neutrino-nucleus cross sections for oscillation experiments. *J. Phys. G* **2018**, *45*, 013001. [[CrossRef](#)]
31. Ankowski, A.M.; Mariani, C. Systematic uncertainties in long-baseline neutrino-oscillation experiments. *J. Phys. G* **2017**, *44*, 054001. [[CrossRef](#)]
32. Benhar, O.; Huber, P.; Mariani, C.; Meloni, D. Neutrino-nucleus interactions and the determination of oscillation parameters. *Phys. Rep.* **2017**, *700*, 1. [[CrossRef](#)]
33. Alvarez-Ruso, L.; Sajjad Athar, M.; Barbaro, M.B.; Cherdack, D.; Christy, M.E.; Coloma, P.; Donnelly, T.W.; Dytman, S.; de Gouvêa, A.; Hill, R.J.; et al. NuSTEC White Paper: Status and challenges of neutrino-nucleus scattering. *Prog. Part. Nucl. Phys.* **2018**, *100*, 1. [[CrossRef](#)]
34. Amaro, J.E.; Barbaro, M.B.; Caballero, J.A.; Donnelly, T.W.; Molinari, A.; Sick, I. Using electron scattering superscaling to predict charge-changing neutrino cross sections in nuclei. *Phys. Rev. C* **2005**, *71*, 015501. [[CrossRef](#)]
35. Amaro, J.E.; Barbaro, M.B.; Caballero, J.A.; González-Jiménez, R.; Megias, G.D.; Ruiz Simo, I. Electron- versus neutrino-nucleus scattering. *J. Phys. G* **2020**, *47*, 124001. [[CrossRef](#)]
36. Amaro, J.E.; Barbaro, M.B.; Caballero, J.A.; Donnelly, T.W.; Gonzalez-Jimenez, R.; Megias, G.D.; Simo, I.R. Neutrino-nucleus scattering in the SuSA model. *Eur. Phys. J. ST* **2021**, *230*, 4321. [[CrossRef](#)]
37. Ankowski, A.M.; Ashkenazi, A.; Bacca, S.; Barrow, J.L.; Betancourt, M.; Bodek, A.; Christy, M.E.; Dytman, L.D.S.; Friedland, A.; Hen, O.; et al. Electron Scattering and Neutrino Physics. *arXiv* **2022**, arXiv:2203.06853 [hep-ex].
38. Rosenfelder, R. Quasielastic electron scattering from nuclei. *Ann. Phys.* **1980**, *128*, 188. [[CrossRef](#)]
39. Serot, B.D.; Walecka, J.D. The Relativistic nuclear many-body problem. *Adv. Nucl. Phys.* **1986**, *16*, 1.
40. Drechsel, D.; Giannini, M.M. Electron scattering off nuclei. *Rep. Prog. Phys.* **1989**, *52*, 1083. [[CrossRef](#)]
41. Wehrberger, K. Electromagnetic response functions in quantum hadrodynamics. *Phys. Rep.* **1993**, *225*, 273. [[CrossRef](#)]
42. Barbaro, M.B.; Cenni, R.; De Pace, A.; Donnelly, T.W.; Molinari, A. Relativistic γ -scaling and the Coulomb sum rule in nuclei. *Nucl. Phys. A* **1998**, *643*, 137. [[CrossRef](#)]
43. Giusti, C.; Meucci, A.; Ivanov, M.V.; Udias, J.M. Relativistic Green's function model and optical potential. *Nucl. Theor.* **2015**, *34*, 34–44.

44. Pandey, V.; Jachowicz, N.; Van Cuyck, T.; Ryckebusch, J.; Martini, M. Low-energy excitations and quasielastic contribution to electron-nucleus and neutrino-nucleus scattering in the continuum random-phase approximation. *Phys. Rev. C* **2015**, *92*, 024606. [[CrossRef](#)]
45. Martini, M.; Jachowicz, N.; Ericson, M.; Pandey, V.; Van Cuyck, T.; Van Dessel, N. Electron-neutrino scattering off nuclei from two different theoretical perspectives. *Phys. Rev. C* **2016**, *94*, 015501. [[CrossRef](#)]
46. González-Jiménez, R.; Nikolakopoulos, A.; Jachowicz, N.; Udías, J.M. Nuclear effects in electron-nucleus and neutrino-nucleus scattering within a relativistic quantum mechanical framework. *Phys. Rev. C* **2019**, *100*, 045501. [[CrossRef](#)]
47. Alberico, W.M.; Ericson, M.; Molinari, A. The Role of Two Particles—Two Holes Excitations in the Spin—Isospin Nuclear Response. *Ann. Phys.* **1984**, *154*, 356. [[CrossRef](#)]
48. Van Orden, J.W.; Donnelly, T.W. Mesonic processes in deep inelastic electron scattering from nuclei. *Ann. Phys.* **1981**, *131*, 451–493. [[CrossRef](#)]
49. Dekker, M.J.; Brussaard, P.J.; Tjon, J.A. Relativistic meson exchange and isobar currents in electron scattering: Noninteracting Fermi gas analysis. *Phys. Rev. C* **1994**, *49*, 2650–2670. [[CrossRef](#)]
50. Martini, M.; Ericson, M.; Chanfray, G.; Marteau, J. Neutrino and antineutrino quasielastic interactions with nuclei. *Phys. Rev. C* **2010**, *81*, 045502. [[CrossRef](#)]
51. Lalakulich, O.; Gallmeister, K.; Mosel, U. Many-Body Interactions of Neutrinos with Nuclei—Observables. *Phys. Rev. C* **2014**, *86*, 014614; Erratum in *Phys. Rev. C* **2014**, *90*, 029902. [[CrossRef](#)]
52. Nieves, J.; Ruiz Simo, I.; Vicente Vacas, M.J. Two Particle-Hole Excitations in Charged Current Quasielastic Antineutrino–Nucleus Scattering. *Phys. Lett. B* **2013**, *721*, 90–93. [[CrossRef](#)]
53. Van Cuyck, T.; Jachowicz, N.; González-Jiménez, R.; Ryckebusch, J.; Van Dessel, N. Seagull and pion-in-flight currents in neutrino-induced $1N$ and $2N$ knockout. *Phys. Rev. C* **2017**, *95*, 054611. [[CrossRef](#)]
54. De Pace, A.; Nardi, M.; Alberico, W.M.; Donnelly, T.W.; Molinari, A. The $2p$ – $2h$ electromagnetic response in the quasielastic peak and beyond. *Nucl. Phys. A* **2003**, *726*, 303–326. [[CrossRef](#)]
55. Ruiz Simo, I.; Amaro, J.E.; Barbaro, M.B.; De Pace, A.; Caballero, J.A.; Donnelly, T.W. Relativistic model of $2p$ - $2h$ meson exchange currents in (anti)neutrino scattering. *J. Phys. G* **2017**, *44*, 065105. [[CrossRef](#)]
56. Martínez-Consentino, V.L.; Simo, I.R.; Amaro, J.E. Meson-exchange currents and superscaling analysis with relativistic effective mass of quasielastic electron scattering from C_{12} . *Phys. Rev. C* **2021**, *104*, 025501. [[CrossRef](#)]
57. Martínez-Consentino, V.L.; Amaro, J.E.; Ruiz Simo, I. Semiempirical formula for electroweak response functions in the two-nucleon emission channel in neutrino-nucleus scattering. *Phys. Rev. D* **2021**, *104*, 113006. [[CrossRef](#)]
58. Benhar, O.; Lovato, A.; Rocco, N. Contribution of two-particle–two-hole final states to the nuclear response. *Phys. Rev. C* **2015**, *92*, 024602. [[CrossRef](#)]
59. Rocco, N.; Lovato, A.; Benhar, O. Unified description of electron-nucleus scattering within the spectral function formalism. *Phys. Rev. Lett.* **2016**, *116*, 192501. [[CrossRef](#)]
60. Rocco, N.; Barbieri, C.; Benhar, O.; De Pace, A.; Lovato, A. Neutrino-Nucleus Cross Section within the Extended Factorization Scheme. *Phys. Rev. C* **2019**, *99*, 025502. [[CrossRef](#)]
61. Nikolakopoulos, A.; Lovato, A.; Rocco, N. Relativistic effects in Green’s function Monte Carlo calculations of neutrino-nucleus scattering. *arXiv* **2023**, arXiv:2304.11772.
62. Amaro, J.E.; Barbaro, M.B.; Caballero, J.A.; Donnelly, T.W.; Molinari, A. Delta isobar relativistic meson exchange currents in quasielastic electron scattering. *Nucl. Phys. A* **2003**, *723*, 181–204. [[CrossRef](#)]
63. Kohno, M.; Ohtsuka, N. Meson exchange current contribution to quasifree electron scattering. *Phys. Lett. B* **1981**, *98*, 335–339. [[CrossRef](#)]
64. Alberico, W.M.; Donnelly, T.W.; Molinari, A. Pionic Effects in Quasielastic Electron Scattering. *Nucl. Phys. A* **1990**, *512*, 541–590.
65. Meucci, A.; Giusti, C.; Pacati, F.D. Meson exchange currents in a relativistic model for electromagnetic one nucleon emission. *Phys. Rev. C* **2002**, *66*, 034610. [[CrossRef](#)]
66. Boffi, S.; Giusti, C.; Pacati, F.D.; Radici, M. Nucleon recoil polarization in electromagnetic quasi-free knockout including two-body currents. *Nucl. Phys. A* **1990**, *518*, 639. [[CrossRef](#)]
67. Boffi, S.; Radici, M. Quasi-elastic electron scattering at high momenta beyond the impulse approximation. *Phys. Lett. B* **1990**, *242*, 151. [[CrossRef](#)]
68. Boffi, S.; Radici, M. Nuclear response in electromagnetic quasi-free knockout including two-body currents. *Nucl. Phys. A* **1991**, *526*, 602. [[CrossRef](#)]
69. Martínez-Consentino, V.L.; Ruiz Simo, I.; Amaro, J.E.; Ruiz Arriola, E. Fermi-momentum dependence of relativistic effective mass below saturation from superscaling of quasielastic electron scattering. *Phys. Rev. C* **2017**, *96*, 064612. [[CrossRef](#)]
70. Amaro, J.E.; Martínez-Consentino, V.L.; Ruiz Arriola, E.; Ruiz Simo, I. Global Superscaling Analysis of Quasielastic Electron Scattering with Relativistic Effective Mass. *Phys. Rev. C* **2018**, *98*, 024627. [[CrossRef](#)]
71. Donnelly, T.W.; Sick, I. Superscaling of inclusive electron scattering from nuclei. *Phys. Rev. C* **1999**, *60*, 065502. [[CrossRef](#)]
72. González-Jiménez, R.; Megias, G.D.; Barbaro, M.B.; Caballero, J.A.; Donnelly, T.W. Extensions of Superscaling from Relativistic Mean Field Theory: The SuSAv2 Model. *Phys. Rev. C* **2014**, *90*, 035501. [[CrossRef](#)]
73. Megias, G.D.; Amaro, J.E.; Barbaro, M.B.; Caballero, J.A.; Donnelly, T.W.; Ruiz Simo, I. Charged-current neutrino-nucleus reactions within the superscaling meson-exchange current approach. *Phys. Rev. D* **2016**, *94*, 093004. [[CrossRef](#)]

74. Ruiz Simo, I.; Martinez-Consentino, V.L.; Amaro, J.E.; Ruiz Arriola, E. Quasielastic charged-current neutrino scattering in the scaling model with relativistic effective mass. *Phys. Rev. D* **2018**, *97*, 116006. [[CrossRef](#)]
75. Amaro, J.E.; Ruiz Arriola, E.; Ruiz Simo, I. Scaling violation and relativistic effective mass from quasi-elastic electron scattering: Implications for neutrino reactions. *Phys. Rev. C* **2015**, *92*, 054607; Erratum in *Phys. Rev. C* **2019**, *100*, 019904. [[CrossRef](#)]
76. Amaro, J.E.; Barbaro, M.B.; Caballero, J.A.; Donnelly, T.W.; Molinari, A. Gauge and Lorentz invariant one pion exchange currents in electron scattering from a relativistic Fermi gas. *Phys. Rep.* **2002**, *368*, 317–407. [[CrossRef](#)]
77. Casale, P.R.; Amaro, J.E.; Martinez-Consentino, V.L.; Simo, I.R. Improved Superscaling in Quasielastic Electron Scattering with Relativistic Effective Mass. *Universe* **2023**, *9*, 158. [[CrossRef](#)]
78. Pascalutsa; Scholten, O. On the structure of the $\gamma N\Delta$ vertex: Compton scattering in the Δ (1232) region and below. *Nucl. Phys. A* **1995**, *591*, 658. [[CrossRef](#)]
79. Sommer, B. Deuteron electrodisintegration at high energy and momentum transfer. *Nucl. Phys. A* **1978**, *308*, 263–289. [[CrossRef](#)]
80. Ericson, T.O.; Weise, W. *Pions and Nuclei*; Oxford University Press: New York, NY, USA, 1988.
81. Llewellyn Smith, C.H. Neutrino Reactions at Accelerator Energies. *Phys. Rep.* **1972**, *3*, 261–379. [[CrossRef](#)]
82. Hernandez, E.; Nieves, J.; Valverde, M. Weak Pion Production off the Nucleon. *Phys. Rev. D* **2007**, *76*, 033005. [[CrossRef](#)]
83. Quiros, J.J.; Barbero, C.; Jaramillo, D.E.; Mariano, A. Different vertex parameterizations and propagators for the Δ contribution in π -photoproduction. *J. Phys. G Nucl. Part. Phys.* **2017**, *44*, 045112. [[CrossRef](#)]
84. Kim, H.C.; Schramm, S.; Horowitz, C.J. Delta excitations in neutrino–Nucleus scattering. *Phys. Rev. C* **1996**, *53*, 2468–2473. [[CrossRef](#)]
85. Hockert, J.; Riska, D.O.; Gari, M.; Huffman, A. Meson exchange currents in deuteron electro-disintegration. *Nucl. Phys.* **1973**, *A217*, 14. [[CrossRef](#)]
86. Benhar, O.; Day, D.; Sick, I. An archive for quasi-elastic electron-nucleus scattering data. *arXiv* **2006**, arXiv:nucl-ex/0603032.
87. Benhar, O.; Day, D.; Sick, I. Available online: <http://faculty.virginia.edu/qes-archive/> (accessed on 5 September 2023).
88. Amaro, J.E.; Lallena, A.M.; Co, G. Finite size effects in the electromagnetic quasi-elastic responses in nuclei. *Int. J. Mod. Phys.* **1994**, *E3*, 735. [[CrossRef](#)]
89. Riska, D.O. Exchange currents. *Phys. Rep.* **1989**, *181*, 207. [[CrossRef](#)]
90. Amaro, J.E.; Barbaro, M.B.; Caballero, J.A.; Kazemi Tabatabaei, F. Semirelativistic meson exchange currents in (e,e-prime) and (e,e-prime p) reactions. *Phys. Rev. C* **2003**, *68*, 014604. [[CrossRef](#)]
91. Casale, P.R.; Amaro, J.E.; Ruiz Arriola, E.; Ruiz Simo, I. Center of mass momentum dependence of short-range correlations with the coarse-grained Granada potential. *arXiv* **2023**, arXiv:2304.00296.
92. Martinez-Consentino, V.L.; Amaro, J.E.; Casale, P.R.; Ruiz Simo, I. Extended superscaling with two-particle emission in electron and neutrino scattering. *Phys. Rev. D* **2023**, *108*, 013007. [[CrossRef](#)]

Disclaimer/Publisher’s Note: The statements, opinions and data contained in all publications are solely those of the individual author(s) and contributor(s) and not of MDPI and/or the editor(s). MDPI and/or the editor(s) disclaim responsibility for any injury to people or property resulting from any ideas, methods, instructions or products referred to in the content.